T.C.
İSTANBUL UNIVERSITY
INSTITUTE OF GRADUATE STUDIES IN SCIENCE AND ENGINEERING

Ph.D. THESIS

ELECTRICAL CHARACTERISATION OF InGaAs/GaAs QUANTUM WELL AND GRAPHENE SEMICONDUCTOR STRUCTURES

ADAL AB. MA. RAJHI

Department of Physics

Physics Programme

SUPERVISOR
Prof. Dr. Ayşe EROL

June, 2021

İSTANBUL

This study was accepted on 28/5/2021 as a Ph. D. thesis in Department of Physics, Physics Programme by the following Committee.

Examining Committee Members

Prof. Dr. Ayşe EROL(Supervisor)
İstanbul University
Faculty of Science

Prof. Dr. Sefer Bora LİŞESİVDİN
Gazi University
Science Faculty

Assoc. Prof. Dr. Ömer DÖNMEZ
İstanbul University
Science Faculty

Prof. Dr. Merih SERİN
Yıldız Teknik University
Science Faculty

Assist. Prof. Dr. Fahrettin SARCAN
İstanbul University
Science Faculty

As required by the 9/2 and 22/2 articles of the Graduate Education Regulation which was published in the Official Gazette on 20.04.2016, this graduate thesis is reported as in accordance with criteria determined by the Institute of Graduate Sttudies in Science and Engineering by using the plagiarism software to which İstanbul University is a subscriber.

FOREWORD

I offer special thanks to my supervisor, Prof. Dr. Ayşe Erol, for what she provided to me during my graduate studies. Also, thanks to Assoc. Prof. Ömer Dönmez for his help and support. I also express my gratitude to Assist. Prof. Saffettin Yıldırım, Assist. Prof. Dr. Fahrettin Sarcan Assoc. Prof. Ferhat Nutku, PhD candidate Mustafa Aydın, and all friend in Nano-Opto Research Group for their help and contributions during my studies.

Special thanks and gratitude to my parents for their continued support.

To my wife and children, whom I have been fortunate enough to have in my life, thanks for patient and unlimited support during my period study.

April 2021 **ADAL AB.MA. RAJHI**

TABLE OF CONTENTS

Page

LIST OF FIGURES

Page

LIST OF TABLES

Pagess

LIST OF SYMBOLS AND ABBREVIATIONS

Symbol	Explanation
μ	: Carrier mobility
n_{2D}	: 2D Carrier concentration
b	: optical bowing parameter
x	: alloy composition
λ_{deB}	: de Broglie wavelength
m^*	: effective mass of particle
m_w^*	: effective mass in the quantum well
m_b^*	: effective mass in the barrier
h	: Plank constant
k_B	: Boltzmann constant
$\hbar$	: Planck constant
E	: Energy
ψ	: Wave function
m_e^*	: Effective mass of electron
N	: Quantum number
n	: Carrier concentration in three dimensions
L	: Quantum well width
k	: Wave vector
κ	: exponential decay constant in the barrier
$\vec{F}$	: Force
e	: Charge of electron
$\overrightarrow{v_d}$	: Drift velocity
Δ	: The lateral length of an interface roughness
Λ	: Correlation length
S_0	: Static screening constant
U_{Al}	: Alloy potential
Ω_0	: Unit cell volume
ε_0	: Dielectric permeability constant of space
ε_s	: Low frequency dielectric constant

a_B : Bohr radius

a_0 : Lattice constant

ρ : Density of crystal

v_L : Longitudinal acoustic phonon velocity

E_{dp} : Deformation potential

b_{FH} : Fang- Howards expression

$J_{dp}(k)$: Deformation potential integral

$J_{pe}(k)$: Piezoelectric potential integral

F(q) : Form factor

ω_{po} : Polar optical phonon frequency

ε_∞ : High frequency dielectric constants

d_1 : Thickness of the spacer layer

a : Carbon–carbon distance

L : Width of the quantum well

$\vec{k}_x$: Wavevector in the *x* direction

$\vec{k}_y$: Wavevector in the *y* direction

$\vec{k}_z$: Wav vector in the z direction

v_F : Fermi velocity

$D(E)$: Density of states

n_{sh} : Sheet carrier density

$f(E)$: Fermi-Dirac distribution function

E_F : Fermi level

C_i : Fitting parameters for coupling strength

E_i : Fitting parameters for phonon energy

D_A : Deformation potential

ρ_s : Mass density of graphene

v_s : Longitudinal acoustic phonon velocity

μ_{SR} : Short range scattering

μ_C : Coulomb scattering

F_L : Lorentz force

l : Length of the main arm at Hall bar

w : Width of the sample

d : Thickness of the sample

N_L : Landau quantum number

ω_c : Cyclotron frequency

ω_G : Cyclotron frequency of graphene

$\hbar\omega_c$: Energy difference between Landau levels

τ_q : Quantum life

μ_q : Quantum mobility

l_B : Length scale of the cyclotron motion

Abbreviation	**Explanation**
2DEG	: Two dimensional electron gas
SLG	: Single-layer graphene
MDH	: Modulation- Doped Heterostructure
CVD	: Chemical-Vapour-deposition
VCA	: Virtual Crystal Approximation (VCA)
BZ	: Brillouin Zone
QW	: Quantum Well

ÖZET

DOKTORA TEZİ

InGaAs/GaAs KUANTUM KUYUSU VE GRAFEN YARIİLETKEN YAPILARIN ELEKTRİKSEL KARAKTERİZASYONU

ADAL AB.MA. RAJHI

İstanbul Üniversitesi

Fen Bilimleri Enstitüsü

Fizik Anabilim Dalı

Danışman : Prof. Dr. Ayşe EROL

Bu tezde, n-tipi modülasyon katkılı $In_{0.32}Ga_{0.68}As/GaAs$ kuantum kuyusu yapılarının (kuazi-iki boyutlu yapılar) ve TiO_2/Si alttaş üzerine büyütülmüş tek katmanlı grafenin (gerçek iki boyutlu) elektronik taşınım özellikleri incelenmiştir. Büyütme sıcaklığının ve ısıl işlemin kuazi-iki boyutlu yapıların elektronik taşınım özelliklerine etkisi de incelenmiştir.

Çalışmanın ilk bölümünde, kuazi iki boyutlu yapılarda 4.2K ile 300K arasındaki sıcaklıklarda Hall Olayı ölçümü kullanılarak elektron mobilitesi ve taşıyıcı konsantrasyonu gibi elektriksel özellikleri belirlenmiştir. Isıl işlem ve büyütme sıcaklığının elektronik taşınım özellikleri üzerindeki etkileri araştırılmış ve taşıyıcıların mobilitesi, yoğunluğu, etkin kütle, alaşım potansiyeli ve arayüz pürüzlülüğü parametreleri açısından etkileri incelenmiştir.

Kuazi iki boyutlu yapılarda ($In_{0.32}Ga_{0.68}As/GaAs$ kuantum kuyusu) baskın saçılma mekanizmalarını belirlemek için, elektron mobilitesinin sıcaklığa bağlı değişimi olası saçıla mekanizmaları dikkate alınarak analitik bir modelle belirlenmiştir.

Manyetotransport ölçümleri 4.2K ile 300K arasında yapılmış ve etkin kütle, Fermi seviyesi ve 2D taşıyıcı yoğunluğu, Shubnikov de Haas (SdH) salınımlarının sıcaklığa bağlı değişimleri analiz edilerek bulunmuştur.

Çalışmanın ikinci bölümünde, TiO_2/Si altaş üzerine kimyasal buhar depolama biriktirme tekniği kullanılarak tek tabaka olarak büyütülmüş grafenin, elektron mobilitesi ve taşıyıcı yoğunluğu gibi elektriksel özellikleri sıcaklığa bağlı olarak Hall olayı ölçümleri ile belirlenmiştir. Sıcaklığa bağlı elektron mobilitesi karakteristiği olası saçılma mekanizmaları dikkate alınarak analitik bir model ile incelenmiştir. Hesaplamalarda boyuna akustik fonon saçılması, uzak arayüz optik fonon saçılması ve sıcaklıktan bağımsız saçılma mekanizmaları kullanılmıştır.

Tüm kuazi iki boyutlu örnekler Tampere Teknik Üniversitesi Optoelektronik Araştırma Merkezi'nde (Finlandiya) Moleküler Demet Epitaksi yöntemi ile büyütüldü. Gerçek iki boyutlu grafen örneğinin büyütülmesi ve fabrikasyonu İhsan Doğramacı-Bilkent Üniversitesi'nde gerçekleştirildi. Kuazi iki boyutlu örneklerin fabrikasyonu İstanbul Üniversitesi, Fen Fakültesi Fizik Bölümü İleri Litografik Yöntemler Laboratuarı, magnetotransport ölçümleri ise Nano ve Optoelektronik Araştırma Laboratuarı ile Yüksek Manyetik Alan ve Düşük Sıcaklık Laboratuvarı'nda yapılmıştır.

Nisan 2021, .71. sayfa.

Anahtar kelimeler: $In_{0.32}Ga_{0.68}As$/GaAs, 2 boyutlu yapılar, grafen, modülasyon katkılı yapılar, elektronik taşınım

SUMMARY

Ph.D. THESIS

ELECTRICAL CHARACTERISATION OF InGaAs/GaAs QUANTUM WELL AND GRAPHENE SEMICONDUCTOR STRUCTURES

ADAL AB.MA. RAJHI

İstanbul University

Institute of Graduate Studies in Science and Engineering

Department of Physics

Supervisor : Prof. Dr. Ayşe EROL

In this thesis, electronic charge transport properties of n-type modulation doped ($In_{0.32}Ga_{0.68}As$/GaAs) quantum well (QW) structures (quasi-2D structures) and single-layer graphene on TiO_2/Si substrate (real-2D) structures were studied. The effects of thermal annealing and growth temperature on electronic transport properties of the quasi-2D structures are also studied.

In the first part of study, the electrical properties of InGaAs/GaAs quasi -2D samples such as Hall mobility and carrier concentration have been determined using Hall effect measurement at temperatures between 4.2K and 300K. The effect of thermal annealing and growth temperature on electronic transport properties have been investigated and compared in terms of carrier mobility, carried density, effective mass, alloy potential and interface roughness parameters.

To determine the dominant scattering mechanisms in the quasi-2D structures ($In_{0.32}$ $Ga_{0.68}As$ /GaAs), temperature dependent Hall mobility results have been analysed using an analytical model, considering all possible scattering mechanisms in the quasi 2D samples.

The magnetotransport measurements was carried out between 4.2K and 300K. The effective mass, Fermi level and 2D carrier density have been calculated by analysing temperature dependence of the amplitude of Shubnikov de Haas (SdH) oscillations.

In the second part of study, the electrical properties of a single-layer graphene grown by Chemical Vapour Deposition (CVD) on TiO_2/Si substrate (SLG/TiO_2 /Si), such as Hall mobility and carrier concentration have been determined by Hall effect measurement at temperatures between 77K and 300K. For explaining the temperature dependence of the carrier mobility. Analytical expressions that given in Section 1.4.2. were used. Longitudinal acoustic phonon scattering, remote interface optical phonon scattering and temperature independent scattering mechanisms were used in the calculations.

All quasi-2D samples In GaAs were grown by Molecular Beam Epitaxy (MBE) at Optoelectronic Research Centre (ORC) of Tampere Technique University, Finland. Graphene sample (SLG / TiO_2 / Si) were grown and fabricated at İhsan Doğramacı-Bilkent University. The fabrication of quasi-2D materials using photolithography was made at Advanced Lithographic Techniques Laboratory and magnetotransport measurements were carried out Nano and Optoelectronics Research Laboratory and High Magnetic Field Low Temperature Laboratory of Department of Physics, Science Faculty, Istanbul University.

April 2021, 71 pages.

Keywords: $In_{0.32}Ga_{0.68}As$/GaAs, 2D structures, graphene, modulation doped structures, electronic transport.

1. INTRODUCTION

With the development of epitaxial growth techniques such as Molecular Beam Epitaxy (MBE) and Metal Organic Chemical Vapor Deposition (MOCVD) in 1960s, it became possible to grow semiconductors very precisely layer by layer in thicknesses of the order of a few nanometers. In addition, thanks to epitaxial growth techniques, by alloying of binary semiconductor compounds, novel semiconductor materials with the desired bandgap can be grown onto the appropriate substrate. Furthermore, it has been also possible to grow novel semiconductors in which the lattice constant can be tuned and the band structure can be adjusted directly or indirectly. With the shrinkage of sample sizes to the nanometer scale, quantum phenomena began to be used to explain observations in semiconductor physics.

When the dimensions of a semiconductor become comparable to the *de Broglie wavelength*, quantum size effects are observed, and electronic/optic properties of semiconductors change due to these effects. Since *de Broglie wavelength* of electrons (~20 – 40nm) in bulk structures is much smaller than the sample sizes, quantum size effects are unlikely to observe in these structures. Quantum size effects have begun to be observed, thanks to the technological advances that make possible to adjust material sizes to be on the nanometer scale. Using epitaxial growth techniques, semiconductors can be grown as alternating epilayers to form heterostructures. The idea to design heterostructures to be used in optoelectronic/electronic device technologies was first suggested in the 1950s by Herbert Kroemer and Zhores Alferov, who were awarded by Nobel Prize in Physics 2000 "*for developing semiconductor heterostructures used in high-speed- and optoelectronics*"[1]. In heterostructures, if the thickness of the narrow band gap semiconductor sandwiched between larger bandgap semiconductors is close to *de* Broglie wavelength of the carriers, the motion of the carriers in the narrow band gap semiconductor is confined in the growth direction and such structures are called as *quasi two dimensional (quasi-2D)* or *quantum well* structures. The quasi 2D structures are widely used in today's optoelectronic and electronic technologies.

In the early 1970s, the attempts of fabricating nanostructures in the search for novel quantum phenomena started [2]. The operation speed of an electronic or optoelectronic device is related to electron mobility, therefore to fabricate faster devices, materials with higher electron

mobility is a priority. In order to make devices operate faster, Esaki and Tsu proposed heterostructures with modulation doped in 1969. Using modulation doped heterostructures (MDH), we can separate the charge carriers from the parent dopant atoms and suppress the effect of ionized impurity scattering, which is dominant mechanism restricting carrier mobility especially at low temperatures [3]. Stormer *et al* [4], introduced a new doping strategy for semiconductor heterostructures, which spatially separates charge carriers from their parent dopant atoms. As a result of spatially further separation of free charge carriers from their ionized parents, carrier mobility can be enhanced drastically. This idea has been first applied very successfully to AlGaAs/GaAs quantum well (QW) structures [4,5] In this quasi 2D structure, AlGaAs with a proper alloy composition formed the barrier layer and a thin GaAs layer was confined by AlGaAs to behave a QW. AlGaAs was n-type doped and the neighboring lower bandgap was undoped. The electrons generated by ionization of dopant atoms in AlGaAs barrier layer moves into the QW material (GaAs) with lower energy states and form 2D electron gas in the proximity of the interface between AlGaAs and GaAs layers. Of the scattering events limiting electron mobility, ionized impurity scattering is dominant scattering mechanisms at low temperatures. Since the separation increases between electrons in QW and ionized impurities in the barrier layer, and electrons are confined in the QW, mobility of 2D electron gas was observed to be higher in MDHs [6]. After the discovery of MDHs, the high electron mobility transistors were fabricated. MDHs also led to observation of some interesting quantum events such as Quantum Hall effect [7]. and Integer Quantum Hall effect [8], therefore these structures are great of importance for understanding fundamental physics of 2D electron gas. Later MDHs have been fabricated based on different material systems such as InGaAs/InAlAs [9] AlGaN/GaN [10], AlInGaN/GaN [11], GaInNAs/GaAs [12] and GaInAs/GaAs [13] , The 2D electron mobility in a AlGaAs/GaAs MDH is observed to be as high as 1 x $10^7 cm^2/Vs$ [14].

In 2004, groundbreaking experiments carried out by Andre Geim and Kostya Novoselov on a unexpectedly 2D crystal form of a single layer graphene [5] , has led to introduce *real 2D material* family and the graphene is the first member of this family. In contrast to quasi-2D semiconductors, whose electronic properties are defined by quasi-particles that are non-relativistic particles with a finite well-defined mass and obey the Schrödinger wave equation, transport of electrons in graphene obey the Dirac Eq., and they behave like massless Dirac fermions. The electron mobility in graphene is expected to be exceptionally high to make possible observation of quantum phenomena even at room temperature [16] . Compared to very

high-tech expensive growth techniques of quasi 2D structures, the simplicity of exfoliation method to have a single layer graphene has been made it accessible for a wide community. Even the first studies have been focused on its interesting electronic properties, discovery of graphene by Novoselov et al. in 2004 [17] has attracted great interest in different research area as a real 2D-dimensional system. Since it is impossible to have graphene at industrial scale using exfoliation method, the production of graphene was achieved using chemical vapor deposition technique in larger sizes [18]. The promising properties such as high electron mobility, its strength, transparency and flexibility have made graphene attractive in studies of electronic [19] and optoelectronic devices [20,21].

The studies on band structure of graphene [22] revealed that a special linear electronic band structure around the corners of the Brillouin region (Dirac points K and $K^{`}$) causes electrons to behave as massless. Thus electrons move at a velocity of $\sim 10^6\ m/s$, travelling for micrometers without scattering even at room temperature [23].The two Brillouin symmetry points ( $K$ and $K^{`}$) are particular importance in the electronic transport [24], as will be clarified in section (2.3.1.2).

In graphene, confinement of carriers into 2D led to observation of phenomena which, was previously seen only at low temperatures in quasi electron gas (2DEG), such as the quantum Hall effect at room temperature. In addition, integer quantum Hall effect could be observed at moderate temperatures. It has been reported that SdH oscillations in graphene show a phase shift of π because of Berry's phase. It was also noted that, even when carrier density goes to zero the conductivity never goes to zero. [22, 25]. Thanks to its extraordinary electronic properties, graphene is proposed as a good candidate for the quantum Hall resistance metrology having better precision and wider application under less strict conditions such as high temperatures, low magnetic fields [26,27].

In this thesis, it is aimed to investigate electronic transport properties of quasi and real 2D semiconductors. To achieve our goal, two kinds of 2D structures will be used: Modulation doped QW structures and real 2D structures.

Electronic transport properties of n-type modulation doped ($Ga_{0.68}In_{0.32}As$/GaAs) QW structures (quasi-2D semiconductor structures) grown at different growth temperatures using

Molecular Beam Epitaxy (MBE) were investigated. The influence of heat treatment on transport properties of quasi-2D samples have been investigated for 600s under annealing temperature 700^{o}C.

The temperature dependences of the carrier mobility (μ) and the carrier concentration (n_{2D}) were determined from Hall effect measurements. An analytical model was used to investigate the temperature dependence characteristic of 2D electron mobility, considering dominant scattering mechanisms that restricts electron mobility as interface-roughness, acoustic phonon scattering, alloy disorder scattering and optical phonon scattering. The interface roughness scattering is typically quantified from the lateral size (Δ), and the correlation length (Λ) [28,14]. Since the exact values of Λ and Δ are unknown, these parameters are selected being adjustable parameters to obtain the best fit with the experimental data.

The effective mass, Fermi level and 2D electron density were calculated from the SdH oscillations in modulation doped $In_{0.32}Ga_{0.68}As/GaAs$.

Electronic transport properties of real 2D material (graphene) have been studied utilising Hall effect measurements. The measurements have been performed on a CVD-growth single-layer graphene on TiO_2/Si substrate (SLG/TiO_2/Si). Hall effect measurement on Hall-bar shaped SLG/TiO_2/Si sample have been made in the temperature range between 77-300K. For explaining the temperature dependence of the carrier mobility. Analytical expressions that given in Section 1.4.2. were used. Longitudinal acoustic phonon scattering, remote impurity phonon scattering, and temperature independent scattering terms were used to analyses temperature dependence of mobility for numerical calculations.

In the first chapter of this thesis, the fundamental properties of quasi and real 2D materials and the transport mechanism of the quasi and real-2D material are introduced. This chapter is divided in two parts. The area covered in the first part (Sections 1.1-1.3) is related to modulation doped QW structures ($In_{0.32}Ga_{0.68}As/GaAs$ QW). And the area covered in second part (Section 1.4) will be the real-2D structure as a single-layer graphene (SLG/TiO_2/Si). In Section 1.1 the modification of band structure is explained introducing conventional III-V semiconductors alloys. In Section 1.2 we introduce the concept of physics of the quasi 2D structures, then we will continue with fundamental principles of modulation doped heterostructures, quantum confinement effect and then density of state function. In Section 1.3,

electronic transport in quasi-2D structures together with the main scattering mechanisms such as acoustic phonon scattering, alloy disorder scattering, interface roughness scattering, remote impurity scattering will be discussed.

In Section 1.4, we start describing crystal and band structure of graphene (real-2D material)) then we present scattering mechanisms such as longitudinal acoustic phonon scattering, remote impurity phonon scattering and temperature independent scattering terms, which are used to explain temperature dependent behavior of the electron mobility in a single layer graphene sample ($SL/TiO_2/Si$). In Section 1.5, physics behind magnetotransport of electrons in 2D structures are briefly explained at low and high magnetic field regimes.

In the second chapter, the used sample structures and experimental techniques wrer given. The second chapter start with sample structures and growth method for quasi and real- 2D structures then continues with fabrication of the samples in Section 2.2. Finally, experimental methods are presented in Section 2.3.

The results of all experimental study and modelling of temperature dependence of electron mobility are present in Chapter 3. The influence of growth temperature and thermal annealing on electronic transport parameters of the quasi 2D samples and the electronic properties of graphene are presented in Chapter 4. The conclusion and recommendations were presented in Chapter 5.

1.1. MODIFICATION OF BANDSTRUCTURE

1.1.1. Conventional III-V Semiconductor Alloys

Alloying of semiconductors typically refers to the mixing of two or more semiconductor compounds to produce ternary or quaternary alloys to introduce novel semiconductors to be able to use for electronic devices such as high electron mobility transistors, field effect transistor and heterojunction bipolar transistors. Semiconductors from group III-V family are crucial materials for semiconductor devices, where III-V compound semiconductors consist of equal composition of elements from column III as Al, Ga, In and column V as As, P, N. Compounds consisting of two elements are called binary such as, compounds consisting of three elements are called ternary like the samples that have studied in the thesis such as $In_{1-x}Ga_xAs$, and compounds consisting of four elements are called quaternary such as $Ga_xIn_{1-x}As_yP_{1-y}$. x *and* y are alloy compositions given as $0 \leq x, y \leq 1$ [30]. Semiconductor alloys and their heterostructures play an important role in quantum systems and in the development of high-performance electronic/optoelectronic devices. Ternary and quaternary alloys obtained mixing bandgaps enable the formation of heterojunctions, which are also essential for the fabricating of high-performance electronic/optoelectronic devices [31].

Figure 1.1 shows bandgap *versus* lattice constant of binary semiconductor compounds. Alloying of two binaries offers the ability to tailor bandgap and lattice constant. The band structure of a novel conventional semiconductor alloy obtained by mixing of the binary semiconductor compounds is well-described using *Virtual Crystal Approximation* (VCA) [32, 33]. The physical properties of semiconductor alloys such as bandgap, lattice constant and effective mass can be determined by VCA, which considers a virtual potential. The virtual potential is an average of the atomic potentials of constituents in the alloy. The alloy composition dependence of the bandgap of an alloy is described by Vegard's law as [34,35]

$$E(A_{1-x}B_x\ C) = xE(AC) + (1-x)E(BC) - bx(1-x) \tag{1.1}$$

where b is the bowing parameter and composition-independent. $E(AC)$ is bandgap of constituent AC binary compound, $E(BC)$ for constituent BC binary compound for ternary alloy $A_{1-x}B_x$.

In Figure 1.1, the lines connecting two binary compounds having one constituent in common give the composition dependent-lattice constant and band gap change of the corresponding ternary compound.

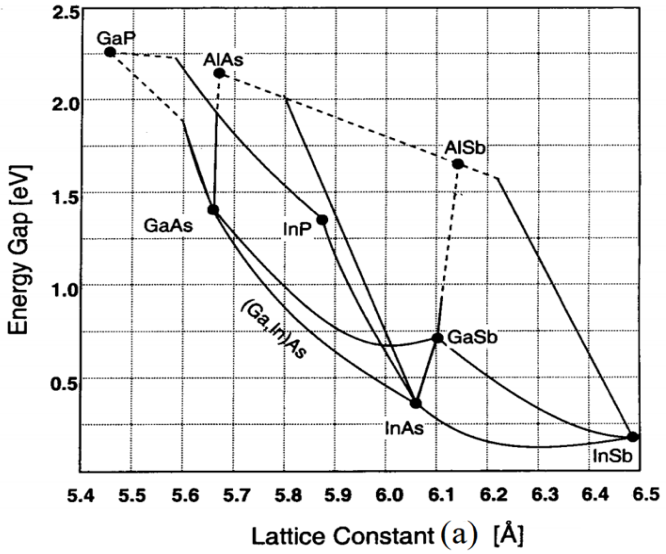

Figure 1.1: Lattice constant *versus* energay gap at room temperature for various III-V binary semiconductor compounds and their alloys. Solid lines represent direct, dashed lines indirect bandgaps [36].

1.2. PHYSICS OF THE QUASI 2D STRUCTURES

Using bandgap engineering strategy, the bandgap of semiconductors can be tailored with alloying of III-V materials such as AlGaAs, InGaAs, which gives opportunity to tune optical and electrical properties of semiconductors. [37]. And semiconductor heterostructures are formed by growing different bandgap materials layer by layer using epitaxial growth techniques to form quantum well-like quasi 2D structures [38].

To obtain high carrier mobility in the semiconductor heterostructures, modulation doped heterostructures are preferred. Modulation doped structures consist of an undoped narrow-gap semiconductor sandwiched with a wider bandgap doped semiconductor. To design this kind of structure, a proper choice of alloy composition presents an advantage to create a novel semiconductor to be used as either narrow or wide bandgap material of a modulation doped heterostructures. The doped wide-gap material behaves as a barrier layer in this structure and surrounds the narrow-gap material. Figure 1.2 shows the band profile of an n-type modulation

doped heterostructure before (a) and after (b) the electron transfer to the narrow bandgap semiconductor, respectively [39].

Considering we have an n-type doped barrier layer, Fermi level will be in close to conduction band edge and for undoped layer, Fermi level will be almost at mid-gap. So, when two different semiconductor materials are brought together, electron will move towards to narrow-bandgap semiconductor, whose conduction band edge is lower energy. Fermi level will go down in wide bandgap semiconductor as a result of losing of electrons, while narrow bandgap semiconductor's Fermi level will go up. At equilibrium state, Fermi level will be equal from left to right and the band profile shown in Figure 1.2b is formed. After free electrons transfer to the narrow bandgap semiconductor, if the thickness of the narrow- bandgap semiconductor is in the range of *de Broglie* wavelength of the electrons or holes, given in Eq. 1.2 [37] , the electron be confined in narrow-bandgap semiconductor. Therefore, transferred electrons form a quantized, 2D electron gas confined in the QW, as shown in Figure 1.2-b. Since electrons are spatially far from their parent ionised impurities, effect of ionised impurity scattering become less as compared to that in doped bulk semiconductors. Therefore, in the modulation doped structures, the electron mobility is enhanced especially at low temperatures, where ionised impurity scattering is the dominant scattering mechanism.

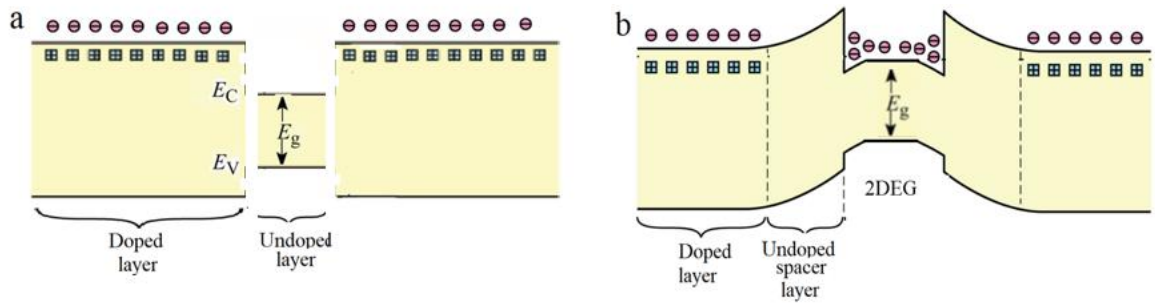

Figure 1.2: Band profile of a doped heterostructure a) before and (b) at equilibrium that electrons transfer to the QW in narrow bandgap semiconductor to form 2DEG.

To increase the distance between electrons and donors further, a spacer layer can be added as seen in Figure 1.2-b. Although the presence of the spacer layer, which work on reduce the electron concentration, in same time it works on increase the carrier mobility. So, the optimum of spacer layer thickness must be adjusted precisely. The quantum confinement effect is

observed when the thickness of the narrow gap semiconductor is between 1-25nm for III-V alloys [40], which is determined from *de Broglie* wavelength of electrons/holes as

$$\lambda_{deB} \sim \frac{h}{\sqrt{m^* k_B T}} \tag{1.2}$$

where λ_{deB}, m^*, h, and k_B are *de Broglie* wavelength of the electrons, effective mass of electron, Planck constant and Boltzmann constant.

The quantum confinement structures are classified according to the number of free dimensions for charge carriers, which are the *quantum well*, *quantum wire* and *quantum dots*. Table 1.1 lists the quantum confined structures together with the number of degrees of freedom associated with the type of quantum confinement.

Table 1.1: Classification of low dimensional structures.

Structure	Quantum confinement	Number of free dimensions	Dependence of energy Electron density of states
Bulk	0	3	$E^{1/2}$
Quantum Well	1	2	E^0
Quantum Wire	2	1	$E^{-1/2}$
Quantum Dot	3	0	δE

A significant difference between the electronic behaviors of bulk and low-dimensional semiconductors comes from their density of states function [41]. Figure 1.3 shows densities of state function as a function of energy. In a bulk semiconductor, the density of states is proportional to $E^{1/2}$, and the electrons in conduction band have any energy above the bandgap energy, E_g at a given temperature. For a QW structure (quasi 2D) , the density of states shifts higher energy than the bandgap of bulk material. In opposite to bulk semiconductor, in QW structure the density of state becomes independent of energy and changes from a continuous dependence to a step-like dependence. Compared with bulk semiconductors, a QW structure has a higher density of c states near conduction and valence bandedges; therefore a higher

density of carriers can contribute to the bandedge emission from a QW based semiconductor laser structure [40]. In quantum wires, the density of states has a $E^{-1/2}$ dependence. In quantum dots, the motion of electrons is quantized in all three directions and there are no continuous bands, the density of state function comprises of a series of Dirac delta (δ)-functions at each quantized level, in which the electrons have discrete energy states [42].

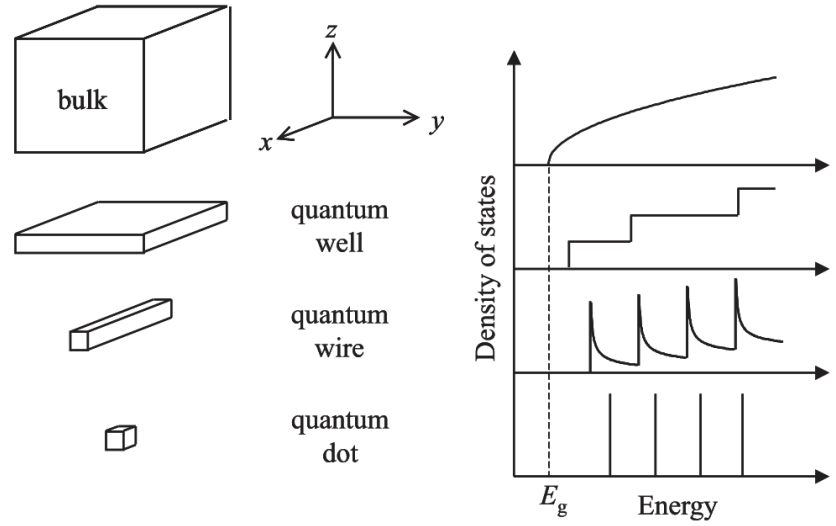

Figure 1.3: Density of states functions of 0D, 1D, 2D and bulk semiconductors [42].

1.2.1 Quantised Energy Levels in Quantum Well Structures

By using the Schrödinger equation and the effective mass approximation, energies of the quantized states and wave functions in the conduction and valence bands of a QW can be obtained [42]. The fundamental properties of a QW can be understood through the simple model particle in a box. So, by considering Schrödinger's equation for (electron or hole) in one dimension, we can study two cases of QWs, infinite well and finite well approximation as we shall see below [43].

$$\frac{\hbar^2}{2m^*}\frac{d^2\psi}{d_z^2} + V(z)\psi = E\psi \tag{1.3}$$

where V(z) is the structural potential (QW potential), z is the growth direction of semiconductor heterostructure, m^* is the effective mass of carrier, E and ψ are the energy and wavefunction.

1.2.1.1. Infinite Potential Wells Approximation

By solving Schrödinger equation for the electrons and holes in the QWs defined by the bandgap discontinuities of a semiconductor heterostructure, the electronic states in QWs can be found [42]. Figure 1.4 a show the simplest case where the barriers on both side of the QW are infinitely high. Schrodinger equation within the QW is:

$$-\frac{\hbar^2}{2m_w^*}\frac{d^2\psi(z)}{L_z^2} = E\psi(z) \tag{1.4}$$

where m_w^* , z and L_z are the effective mass of electron in the QW, the growth direction and is the width of the QW. As we mentioned, in this case, the potential barriers are infinitely high, so there can be no penetration into the barriers, which means the wavefunction must be zero at the barrier of the QW, so $\psi(z) = 0$ and ∞ elsewhere.

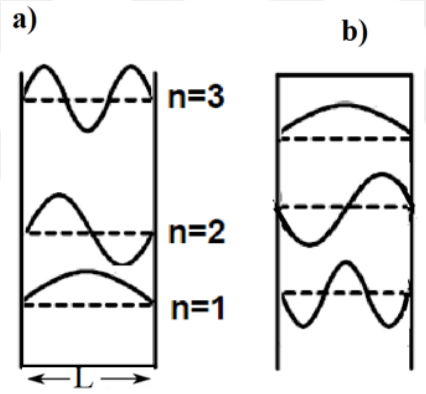

Figure 1.4: Energy levels and wavefunctions of a) electron and b) hole in an infinite QW**.**

We choose the width of the well from $z = 0$ to $z = L$, the normalized wave functions take the form ,

$$\psi_n(z) = \sqrt{\frac{2}{L}}\ sin(k_n z) \tag{1.5}$$

and

$$k_n = \frac{N\pi}{L} \tag{1.6}$$

where N is an integer that gives the quantum number of the state, and the energy E_N that corresponds to the N^{th} level is given by:

$$\mathrm{E_N} = \frac{\hbar^2 \mathrm{k_N^2}}{2\mathrm{m_w^*}} = \frac{\hbar^2}{2m_w^*}\left(\frac{\mathrm{N\pi}}{\mathrm{L}}\right)^2 \tag{1.7}$$

From Eq. 1.7 we can see clearly that the energy levels are inversely proportional with both square of the well width, L, and the effective mass m_w^*, which means that narrower QWs have the higher quantized energies.

1.2.1.2. Finite Potential Wells Approximation

Now by taking a look to a realistic QW that has a finite potential barrier of height V_0 at each interface, which is known as the actual finite well, as shown in Figure 1.5 We can note that there are only a finite number of bound states with energy $E < V_0$. These bound states are labelled by a quantum number N. Inside the QW there is no change in Schrödinger equation. Whereas, inside the barrier the wave equation becomes

$$-\frac{\hbar^2}{2m_b^*}\frac{d^2\psi(z)}{L_z^2} + V_0\psi(z) = E\psi(z) \tag{1.8}$$

where m_b^* refers to effective mass inside the barrier layer. The boundary conditions tell us that the wave function $\psi(z)$ in addition to particle flux $(\frac{1}{m^*})\frac{d\psi}{Lz}$ at the interface must be continuous which gives the series [42]

$$\tan\left(\frac{kL}{2}\right) = \frac{m_w^*\kappa}{m_b^* k} \tag{1.9}$$

$$\tan\left(\frac{kL}{2}\right) = -\frac{m_b^* k}{m_w^*\kappa} \tag{1.10}$$

where, k is the wavevector in the QW, and given by

$$\frac{\hbar^2 k^2}{2m_w^*} = E_n \tag{1.11}$$

and κ is the exponential decay constant in the barrier and it is given by

$$\frac{\hbar^2\kappa^2}{2m_b^*} = V_0 - E_n \tag{1.12}$$

The solution of Eqs. 1.9 and 1.10 can be found by simple numerical methods [42].The wavefunctions in Figure 1.5 are approximately sinusoidal inside the QW, whereas they decay exponentially in the barriers, as seen Figure 1.5. The spreading of the wavefunctions into the barrier by tunnelling increases *k* and lead to reduce the quantum confinement energy compared to a QW with infinite barriers. No matter how small V_0, always we have a finite number of solutions, at least one. From Figure 1.5 a – b, the wave function of the first two states of both infinite well and finite QW apparent [31]. The difference is that the wave functions of the finite QW spreads out more by tunnelling into the barrier, whereas the wave functions of the infinite QW becomes zero at the interfaces.

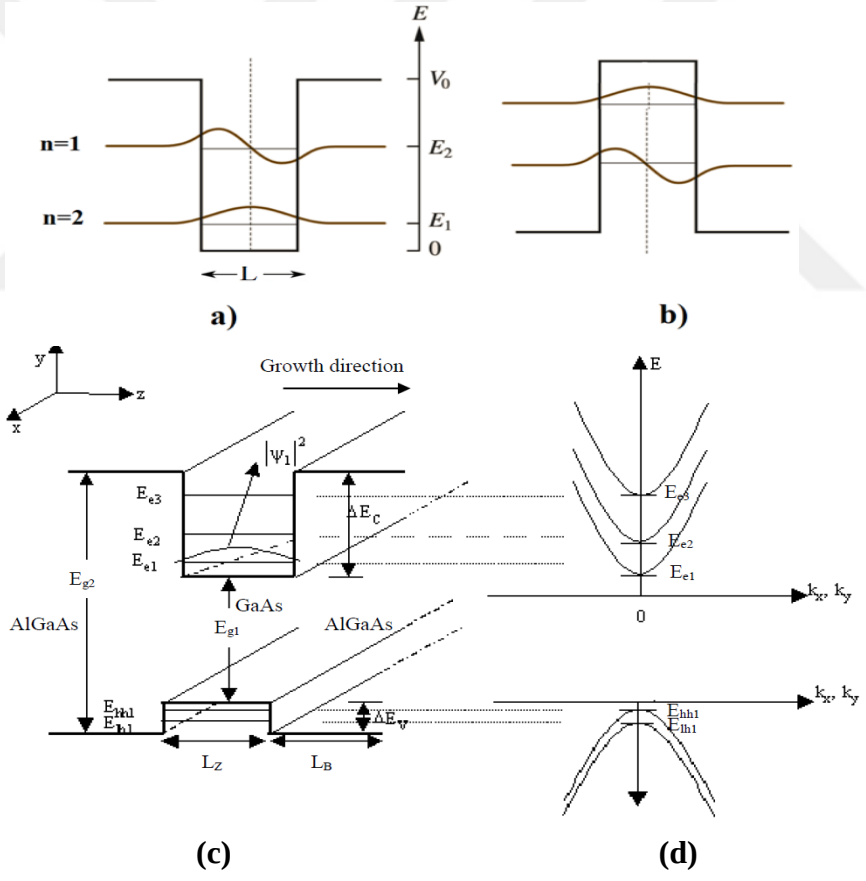

Figure 1.5: Energy level and wave function of a) electrons and b) holes in finite quantum well c) 3D illustration of a AlGaAs/GaAs QW structure and electron and hole subbands in conduction and valance band QWs. E_{e1}, E_{e2} ad E_{e3} are the electron subbands, E_{hh1} and E_{lh1} are the hole subbands. ΔE_C and ΔE_V are conduction and valnce band discontinuties, respectively [31].

A 3D illustration of a GaAlAs/GaAs QW quasi 2D structure composed of two semiconductors with energy band gaps E_{g1} and E_{g2} is illustrated in Figure 1.5c. As a result of quantum confinement effect, the electron and hole subband energy levels become discrete and the separation between adjacent electron/hole subbands are much larger than k_BT, therefore distribution of electrons/holes are not affected by thermal energy.

1.3. ELECTRONIC TRANSPORT IN QUASI 2D STRUCTURES

After applying electric field on a conductor or semiconductor material the carriers in the material speed up till run into a scattering centre. The scattering centres influence transport characteristics of the materials. To explain transport phenomena, it is necessary to know the motion of the carriers under an applied electric field and the scattering mechanisms that may occur during this motion.

1.3.1. Movement of Electron in an Electric Field

Under an applied electric field, e electron experiences electrical force

$$\vec{F} = -e\vec{E} \tag{1.13}$$

and then one can define drift velocity-electric field relation as [39]

$$\overrightarrow{v_d} = -\frac{e\tau}{m_e^*}\overrightarrow{E} \tag{1.14}$$

where τ is the relaxation time, and the mobility of the free carrier can be written from Eq. 1.14 as

$$\mu = -\frac{e\tau}{m_e^*} \tag{1.15}$$

As we see from Eq. 1.15, mobility is inversely proportional to the effective mass of the carriers, whereas changes in direct proportion with the relaxation time. The effect of each kind of scattering centre can be expressed by using the formula developed by Matthiessen [39] as:

$$\frac{1}{\mu} = \sum_i \frac{1}{\mu_i} \tag{1.16}$$

i represent different scattering mechanisms. Each scattering mechanism is described in following subsections.

1.3.2. Scattering Mechanisms

In this section, several scattering mechanisms such as *acoustic phonon scattering* (μ_{Aph}), *alloy disorder scattering* (μ_{Alloy}), *interface roughness scattering* (μ_{ifr}), *remote impurity scattering* (μ_{ri}), which play main role in determination of the carrier mobility in a semiconductor, will be discussed.

1.3.2.1. Interface Roughness Scattering

In layered structures such as modulation doped structures, interface roughness scattering is a vital scattering mechanism due to an imperfection at the interface between different materials. Because the sample is grown layer by layer and the layers are constituted of different materials with different lattice constants, so there will be roughness at the interface between the layers, which gives rise to interface scattering as shown in Figure 1.6. Where, interface roughness scattering mobility can be write as, [44]

$$\mu_{Ir} = \left(\frac{2\varepsilon_0\varepsilon_s}{n_{2D}\Delta\Lambda}\right)^2 \frac{\hbar^3}{e^3 m^{*2}} \frac{1}{j_{Ir}(k)} \tag{1.17}$$

Here n_{2D} is the 2D carrier density, and Δ is the lateral size of the interface roughness, Λ is the correlation length between fluctuations.

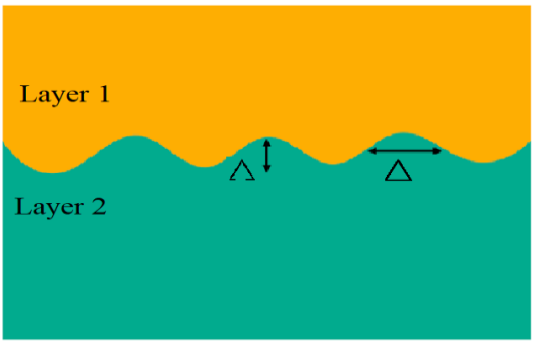

Figure 1.6: The roughness at the interface between the layers with Δ and Λ.

The integral J_{Ir} (k) is given by [28]

$$J_{Ir}(k) = \int_0^{2k} \frac{e^{-q^2\Lambda^2/4}}{2k^3(q+q_{2D})\sqrt{1-\left(\frac{q}{2k}\right)^2}}\, q^4 dq \tag{1.18}$$

where $q = 2\sin(\theta/2)$, θ is the scattering angle and the 2D inverse screening length q_{2D} can be expressed by

$$q_{2D} = \frac{e^2 m^*}{2\mu\hbar^2\varepsilon_0\varepsilon_s}\, F(q) \tag{1.19}$$

Here the form factor F(q) defined by [45]

$$F(q) = \int_0^{\infty} dz \int_0^{\infty} dz' \, [f(z)]^2 \, [f(z')]^2 \, e^{-q|z-z'|} \tag{1.20}$$

1.3.2.2. Alloy Disorder Scattering

It is caused by potential fluctuations due to the random distribution of the atoms forming alloy in crystal [39]. Also, it is found in all semiconductor alloys like $In_xGa_{1-x}As$, and $Ga_{1-x}In_xN_yAs_{1-y}$. The alloy disorder scattering-restricted mobility in an alloy of $A_{1-x}B_xC$ is given by [46]

$$\mu_{Al} = \frac{16\ e\hbar^3}{3bx(1-x)m^{*2}\Omega_0 U_{Alloy}^2} \tag{1.21}$$

where x is the alloy content, the primitive cell volume, Ω_0, the effective mass of the carrier, m^* , for ternary alloys, the potential alloy, U_{Alloy} [46] , and factor b_{FH} is the Fang-Howard expression expressed as [28]

$$b_{FH} = \left(\frac{33e^2\, m^* n_{2D}}{8\varepsilon_0\varepsilon_s\hbar^2}\right)^{1/3} \tag{1.22}$$

where ε_0 is static dielectric constant *and* ε_s dielectric permeability constant of semiconductor,

For N-free ternary alloys, the alloys potential derives by Littlejohn et al as [44,47]

$$U_{A_{1-x}B_xC} = \frac{b}{4\pi\varepsilon_0}\left[\frac{Z_A}{r_A} - \frac{Z_B}{r_B}\right]e^{-k_s R} \tag{1.23}$$

Here Z_A, Z_B, r_A, r_B and R are the valence numbers, covalent radius and the bond length between A and B atoms, respectively. k_s is Thomas-Fermi screening wavenumber and given by

$$k_s^2 = \frac{1}{4}\left(\frac{\pi}{3}\right)^{1/3}\frac{a_B}{n_0} \tag{1.24}$$

where, n_0, a_B are the valence electron density and Bohr radius, respectively. n_0 is given by

$$n_0 = \frac{32}{a_0^3} \tag{1.25}$$

Here the lattice constant a_0 and R of an ternary alloy are defined by Vegard's law as

$$a_0 = (1-x)a_A + xa_B \tag{1.26}$$

$$R = \frac{1}{2}[r_C + xr_B + (1-x)]r_A \tag{1.27}$$

where r_C is the covalent bond radius of the third atom in the alloy.

1.3.2.3. Acoustic Phonon Scattering

The acoustic phonons divided into two branches, transverse and longitudinal acoustic phonons, depending on the transverse and longitudinal oscillations of atoms. The acoustic phonon scattering increases with temperature, because density of phonons increases at higher temperature according to Bose-Einstein statistics [39].

Acoustic phonons scatterings can be categorized as being deformation potential scattering and piezoelectric scattering. The deformation potential limited mobility is defined by Ridley *et al.*[28] as

$$\mu_{dp} = \frac{16\,\rho\, e\, v_L^2 \hbar^3}{3E_{dp}^2 k_B\, Tm^{*2} b_{FH}} \frac{1}{J_{dp}(k)} \tag{1.28}$$

where $\rho,\ E_{dp}\ , v_L\ , b_{FH}$ are the crystal density, deformation potential, longitudinal acoustic phonon velocity and Fang- Howards expression whereas, the $J_{dp}(k)$ is given as

$$J_{dp}(k) = \int_0^{2k} \frac{1}{2\pi k^3\ (q + q_{2D})^2 \sqrt{1 - \left(\frac{q}{2k}\right)^2}} q^4 dq \tag{1.29}$$

where q_{2D} is given in Eq. (1.19).

The mobility limited by piezoelectric scattering is defined as [44] .

$$\mu_{pe} = \frac{\pi \varepsilon_0 \varepsilon_s \hbar^3 k}{e K_{av}^2 k_B\, Tm^{*2}} \frac{1}{J_{pe}(k)} \tag{1.30}$$

Here K_{av} is average electromechanical coupling constant and $J_{pe}(k)$ is defined by the integral as

$$J_{pe}(k) = \int_0^{2k} \frac{F(q)}{4k^2\ (q + q_{2D})^2 \sqrt{1 - \left(\frac{q}{2k}\right)^2}} q^3 dq \tag{1.31}$$

1.3.2.4. Polar Optical Phonon Scattering

Optical phonon scattering becomes more effective at higher temperatures. The mobility restricted by polar optical phonon scattering is expressed as [49].

$$\mu_{po} = \frac{4\pi \varepsilon_0 \varepsilon_p \hbar^2}{e \omega_{po} m^{*2}\, L} \left[exp\left(\frac{\hbar \omega_{po}}{k_B\, T}\right) - 1 \right] \tag{1.32}$$

Here, $\hbar\omega_{po}$ polar optic phonon energy, ε_p is defined as

$$\varepsilon_p = \left[\frac{1}{\varepsilon_\infty} - \frac{1}{\varepsilon_s}\right]^{-1} \tag{1.33}$$

where ε_∞ high frequency dielectric constants.

1.3.2.5. Remote Ionized Impurity Scattering

Remote ionized impurity scattering is caused by ionized doping atoms and is a Coulombic interaction between charge carriers in the QW and the ionised impurities in the barrier layer. Compared to the ionised impurity scattering, remote one is less effective scattering mechanism in modulation-doped structures, where dopant atoms and carriers are spatially distant from each other, thus reducing scattering and improving electron mobility. Limited mobility by scattering of remote ionized impurity atoms is expressed as [44]

$$\mu_{Ri} = \left(\frac{64\pi\hbar\varepsilon_s S_0^2\,(2\pi n_{2D})^{3/2}}{e^3 m^*}\right)^2 \left[\frac{1}{L^2} - \frac{1}{(d_1+L)^2}\right]^{-1} \tag{1.34}$$

where d_1, L and S_0 are the spacer layer thickness, QW width and static constant, respectively. S_0 is defined by two different expressions for degenerate and non-degenerate conditions. For non-degenerate systems, the screening constant is defined as [49]

$$S_0 = \frac{e^2 n}{2\varepsilon k_b T} \tag{1.35}$$

where n is the carrier concentration in three dimension. For degenerate states, it is expressed as

$$S_0 = \frac{e^2 m^*}{2\pi\varepsilon\hbar^2} \tag{1.36}$$

1.4. GRAPHENE: A REAL 2D MATERIAL

Graphene is a real 2D structure of carbon atoms arranged in hexagonal rings, which form a honeycomb lattice. In this structure, $a = 1.42\ A^o$ represent distance between two neighbor carbon atoms. Graphite with different several number of carbon layers that is 3D form of graphene has a different electronic band structure. Here just band structure of a monolayer graphene will be discussed.

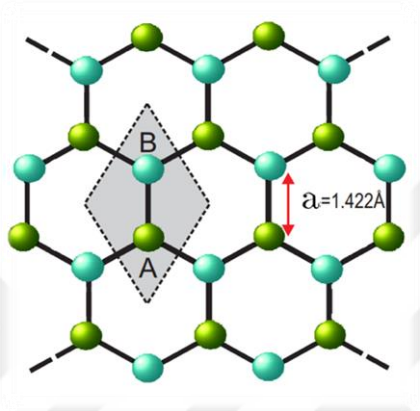

Figure 1.7: Structure of the hexagonal lattice of graphene. Different colours of carbon atoms indicate the two identical sublattices, the basis atoms of the crystal for each sublattice are labelled A and B and a describes the distance between neighbouring carbons [50,51].

1.4.1. Lattice and Band structure of Graphene

1.4.1.1. Lattice Structure of Graphene

To understand graphene properties, it is essential to understand the properties of the carbon atom. And by taking a look on the electronic configuration of carbon, that consist of $1s^2 2s^2 2p^2$ orbitals. Where, electrons in $1s^2$ orbital is essentially inert, and are known as nuclear electrons and do not share in the conduction process. While the other four outer electrons $2s^2 2p^2$ are weakly bonded and known as valence electrons. The valence electrons in the crystalline form occupies $2s, 2p_x, 2p_y$ and $2p_z$ orbitals These orbitals form covalent bond in graphene. Since energy difference between $2s$ and $2p$ levels is small compared to the binding energy of the chemical bonds, the wavefunctions of these four electrons can mix to enhance the binding energy of C-C bonds [22, 52].

Only three orbitals $2s, 2p_x$ and $2p_y$ combine together to form three new equivalent orbitals, with one electron in each orbital. As shown in Figure 1.8a, in-plane of $2s, 2p_x$and $2p_y$ orbitals form strongly coupled $\sigma-$bonds. This operation called as $2p^2$ hybridization. Where, $2p^2$ form three σ- bonds with three nearest neighbor C atoms with angle $120°$ between bonds [22]. Also, the strength of the $\sigma-$ bonds make the graphene one of the strongest materials. The p_z orbital, which has one electron that distributed perpendicular to C atoms plane to form the π- bonds with one of three nearest-neighbour C atoms as shown in Figure1.8b. Interaction between the atoms split the energy levels of π electrons into two bands: the lower $\pi-$ bonding band and the upper $\pi-$ antibonding band [53]. While the lower $\pi-$bonding band forms the valence band the upper π-antibonding bond forms the conduction band of graphene. The valence band and the conduction band are at the at two corners K and $K`$ of the first Brillouin zone (BZ), which is named as Dirac points, as will be explained below.

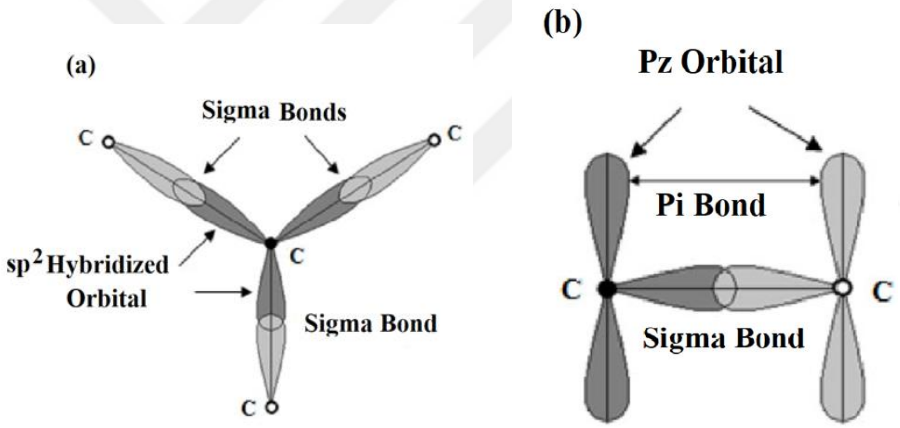

Figure 1.8: a) Sigma bonds formed with sp^2 hybridized orbitals of carbon atoms at angles of 120° b) π-bonds with electrons distributed perpendicular to the molecular plane [22].

As shown in Figure 1.9a, C atoms in graphene are crystalized in hexagonal structure. The structure can be thought of as a triangular lattice with a basis of two atoms *per* unit cell. We note two inequivalent of C atoms, here labelled *A* and *B*, as seen in Figure 1.9a. The lattice vectors can be defined as [54,55],

$$a_1 = \frac{a}{2}(3, \sqrt{3}) \quad \text{and} \qquad a_2 = \frac{a}{2}(3, -\sqrt{3}) \tag{1.37}$$

where $a \approx 1.42$ Å represent the distance between two C atoms. As shown in Figure 1.9b, the reciprocal lattice vectors are given by

$$b_1 = \frac{2\pi}{3a}(1,\sqrt{3}), \qquad b_2 = \frac{2\pi}{3a}(1,-\sqrt{3}) \tag{1.38}$$

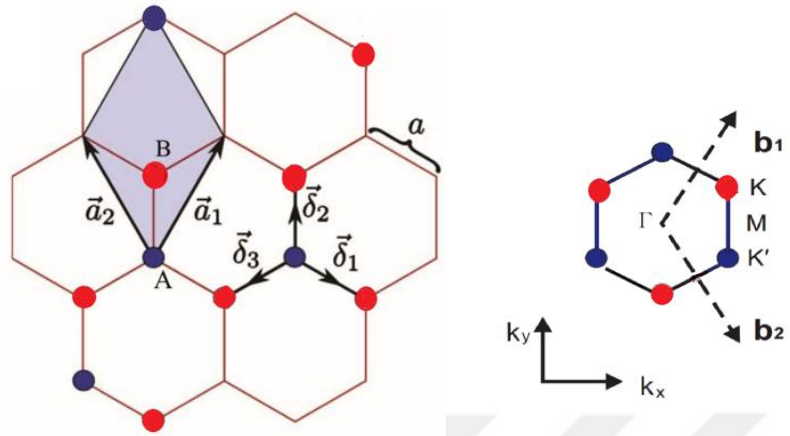

Figure 1.9: a) Hexagonal crystal lattice in graphene with sublattice *A* and *B*. b) The first BZ in the reciprocal lattice with *K* and *K`* points [51].

The Dirac points *K* and *K`* at the corners of the BZ of graphene are of great importance in the electronic transport properties of graphene, as will be clarified in Section 1.4.1.2. The position of Dirac points in *k*- space is defined as [56].

$$K = \left(\frac{2\pi}{3a}, \frac{2\pi}{3\sqrt{3}a}\right), \qquad K` = \left(\frac{2\pi}{3a}, -\frac{2\pi}{3\sqrt{3}a}\right) \tag{1.39}$$

Also, in real space, the three nearest-neighbour vectors δ_1 are given by [57]

$$\delta_1 = \frac{a}{2}(1,\sqrt{3}), \qquad \delta_2 = \frac{a}{2}(1,-\sqrt{3}), \qquad \delta_3 = -a(1,0) \tag{1.40}$$

1.4.1.2. Band structure of Graphene

Wallace in 1947 calculated the electronic bandstructure of graphene [58] using a tight-binding Hamiltonian. The dispersion of bandstructure derived from Hamiltonian is [55]

$$E^{\pm}(k) = \pm t\sqrt{3 + f(k)} - t_{nex} f(k) \tag{1.41}$$

where the (+) and (-) signs refer to the conduction band and valence band of graphene, respectively. t and t_{nex} are the nearest neighbour and next nearest neighbour hopping energy, respectively.

$$f(k) = 2cos\left(\sqrt{3}\, k_y\, a\right) + 4cos\left(\frac{\sqrt{3}\, k_y\, a}{2}\right) cos\left(\frac{3k_x a}{2}\right) \tag{1.42}$$

where k_x and k_y are the components of the wavevector $\vec{k}$. Figure 1.10a shows the cone-like conduction band and the inverted cone-like valence band and the six points where they are touch each other in the BZ (Dirac points). From symmetry consideration, they are equivalent to two points K and $K`$ in the *k*-space, as depicted in Figure 1.9b. The dispersion curve at Figure 1.10b exhibits two important points. First, conduction band minimum and valence band maximum in graphene touches leading to zero bandgap. Second important point is that, by applying the low energy approximation, which is valid near Dirac points, Eq. (1.41) reduces to [22]

$$E^{\pm}(k) \cong \pm\hbar|\vec{q}|v_F \tag{1.43}$$

where $\hbar\vec{q} = \hbar\left(\vec{k} - \vec{K}\right)$ is the electron momentum defined with respect to the Dirac point, v_F is Fermi velocity of carrier in graphene ($1 \times 10^6 ms^{-1}$) [22]. Eq. 1.43 indicates that graphene has a linear dispersion relation at around Dirac points. The linear characteristic of dispersion relation is ascribed for zero- mass particles like the photons. Therefore, it can be concluded that electrons behave like massless Dirac fermions and move with Fermi velocity in graphene.

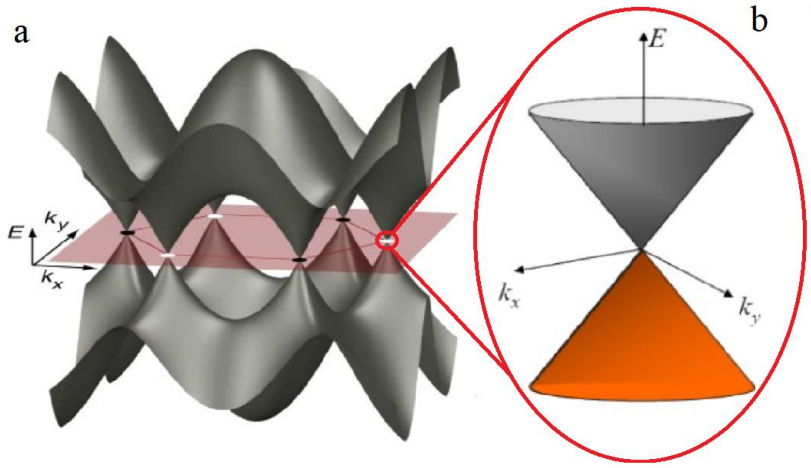

Figure 1.10: Bandstructure of graphene calculated by tight-binding method a) energy dependence on wavevector kx and ky and b) the low energy dispersion relation near Dirac point [56].

At a finite temperature, the conduction and valance bands are occupied with electrons and holes in graphene, as in a bulk semiconductor, respectively. To find the 2D sheet density of such intrinsic carriers in graphene, the linear density of states (DOS) has to be defined. The linear DOS in graphene is [59,60]

$$D(E) = \frac{2|E|}{\pi(\hbar v_F)^2} \tag{1.44}$$

The sheet density (n_{sh}) of 2D electron gas (2DEG) in graphene can be described as [59]

$$n_{sh} = \int_0^\infty dE\, D(E) f(E) \tag{1.45}$$

Fermi-Dirac distribution function $f(E)$given by

$$f(E) = \frac{1}{1+e^{(E-E_F)/k_B T}} \tag{1.46}$$

where k_B , E_F and T are Boltzmann constant, Fermi level and temperature, respectively. By integrating the formula in Eq. 1.45 for electrons and holes at room temperature and taking Fermi velocity v_F in graphene we get

$$n_{2D} = p = n_i = \frac{\pi}{6}\left(\frac{kT}{\hbar v_F}\right)^2 \tag{1.47}$$

where $p, and\ n_{2D}$ are hole and electron concentration, respectively. Eq. 1.47 indicates that the carrier concentration in 2D graphene dependences on only one parameter, the Fermi velocity.

1.4.2. Scattering Mechanisms in Graphene

In order to analyse temperature dependency characteristic of the electron mobility in a single layer graphene, temperature independent mobility (μ_0), longitudinal acoustic phonon scattering (μ_{LA}) and remote interface phonon (μ_{RIP}), were considered.

1.4.2.1. Remote Interfacial Phonon Scattering (μ_{RIP})

Optical phonon energy of the graphene is determined as 0.1 eV [44] that is very high compared with thermal energy at room temperature. Therefore, it is expected that the effect of the optical phonons on electronic transport is very limited. If optical phonon energy in substrate material is close to the thermal energy at a given temperature, optical phonon in substrate layer may affect the electron mobility in graphene layer [61]. The charge carriers are scattered by optical phonons in the substrate and these phonons are known as remote interface phonons (μ_{RIP}), and is given by [62] ,

$$\mu_{RIP} = \frac{1}{n_{2D}e}\left[\sum_i \left(\frac{C_i}{e^{\left(E_i/K_BT\right)} - 1}\right)\right]^{-1} \tag{1.48}$$

where n_{2D} is carrier concentration, phonon energy,E_i , and fitting parameters for coupling strength, C_i .

1.4.2.2. Longitudinal Acoustic Phonon Scattering (μ_{LA})

The lack of piezoelectric and polar-optical phonon scatterings is one of the best advantages in graphene over conventional quasi 2D structures, which they are affected by these two dominant mechanisms at low temperatures and above approximately 100K, respectively. So, here we calculate graphene mobility only considering acoustic phonon scattering through weak deformation-potential coupling, which has been reported between 10 and 30 eV in the literature [61] .

The longitudinal acoustic phonon scattering limited mobility (μ_{LA}), in graphene can be given as [63] ,

$$\mu_{LA} = \frac{4e\hbar\rho_s v_s^2 v_F^2}{n_{2D}\pi D_A^2 k_B T} \tag{1.49}$$

where ρ_s , v_F , D_A , v_s are mass density of graphene Fermi velocity, deformation potential and longitudinal acoustic phonon velocity in graphene.

1.4.2.3. Temperature Independent Scattering Mechanisms (μ_0)

Using Matthiessen's rule, we can find short range scattering (μ_{SR}) and Coulomb scattering (μ_C), which are temperature independent mechanism

$$\frac{1}{\mu_0} = \frac{1}{\mu_{SR}} + \frac{1}{\mu_C} \tag{1.50}$$

where $\mu_{SR} = {}^{A}/_{n_{2D}}$ and $\mu_{C=} S$ [62] where A and S are fitting parameters determined by the short range and Coulomb scattering mechanisms. In contrast to Coulomb scattering which is independent, the short-range scattering inversely dependent to carrier density [64].

1.4.2.4. Ionized impurity scattering (μ_{ii})

Ionized impurity scattering is the process of elastically scattering from some scattering centres. According to Brooks-Herring model [62]

$$\mu_{ii} = \frac{128\sqrt{2\pi}\varepsilon_s^2\varepsilon_0^2(k_B T)^{3/2}}{N_i e^3\sqrt{m^*}} \left[\ln(1+b) - \frac{b}{1+b}\right]^{-1} \tag{1.51}$$

where

$$b = \frac{24m^*\varepsilon_s^2\varepsilon_0^2 k_{BT^2}^2}{N_{3D}e^2\hbar^2} \tag{1.52}$$

where ε_0 permeability of empty space,ε_s static dielectric constant, N_i ionized impurity density and N_{3D} three-dimension carrier density.

1.5. MAGNETOTRANSPORT

In the presence of magnetic fields, electrical measurements provide important information to examine the electronic band structure and electrical properties of the semiconductors. Also, the magnetic field causes significant events in low dimensional semiconductor systems. For example, under a low magnetic field, Hall Effect measurements provide information about semiconductor's carrier type, carrier concentration and carrier mobility. Under high magnetic fields, by examining the change of the amplitude of SdH oscillation depending on temperature gives information about effective mass, quantum mobility and Fermi level of 2DEG [58] .

1.5.1. Low Field Regime: Classical Hall Effect

Although Hall effect was discovered in 1879 by Edwin Hall [65], a full understanding of the Hall effect in metallic conductors only came with the quantum theory of metals. The carrier concentration and carrier mobility in a material can be determined under applied electric and magnetic field using the Hall effect. The type of semiconductor (n- or p-type) can also be determined by Hall effect.

To carry out Hall effect measurements, at least four contacts are needed to apply the electric field and measure Hall voltage. A common geometry used to conduct Hall effect measurement is called Hall bar shape and is shown in Figure 1.11.

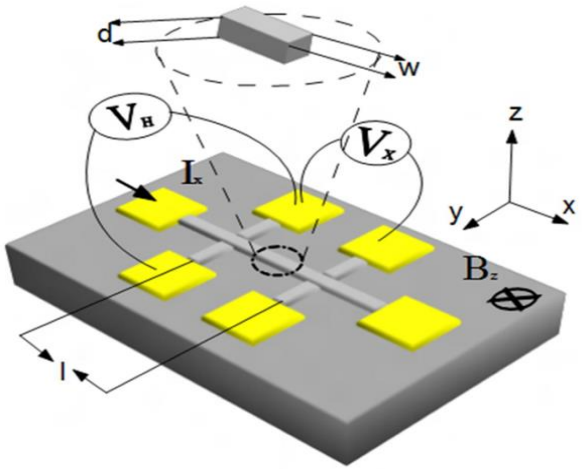

Figure 1.11: Standard Hall bar geometry for Hall Effect measurement. w , d and l are the width, thickness and length of the sample, respectively [49] .

When an electric field is applied in the x-direction, the carriers start moving with the *v* drift velocity along the main arm. When a magnetic field is applied in the z- direction perpendicular to the electric field, an electric field is created in the y- direction, being perpendicular to the directions of electric field and magnetic field. Electrons move under the effect of the Lorentz force (F_L). In the steady-state, the electrical force generated by this electric field and the magnetic force are equal to each other

$$F_L = ev_x \,.\, B_z \; = eE_H \tag{1.53}$$

The current passing through the sample in x-direction is

$$i_x = \sigma E_x wd \tag{1.54}$$

where E_x is the electric field applied in the x-direction and σ is the conductivity, which is defined by

$$\sigma = ne\mu_e + pe\mu_h \tag{1.55}$$

where $n,\ \mu_e\ , p\ , \mu_h$ are concentration of electrons, electron mobility, concentration of holes and Hall mobility in material, respectively. Hall mobility is defined in terms of drift mobility and applied electric field as

$$\mu_h = \frac{v_x}{E_x} \tag{1.56}$$

Using Eq. 1.55 and 1.56 in 1.56, current passing through the sample is expressed as

$$i_x = ne\mu_H E_x wd \; = ne\; v_x wd \tag{1.57}$$

When drift velocity in 1.57 is substituted in 1.53, Hall electric field is obtain as

$$eE_H = \frac{i_x\, B_z}{nwd} \tag{1.58}$$

When the Hall electric field is written in term of Hall voltage V_H, we find

$$\frac{i_x B_z}{nwd} = e\frac{V_H}{w} \tag{1.59}$$

From Eq. 1.59, the Hall potential is defined as

$$V_H = \frac{1}{ned} i_x B_z \tag{1.60}$$

$\frac{1}{ne}$ in Eq. 1.60 is called Hall coefficient (R_H) or Hall resistance. In Eq. 1.60, n is carrier concentration in three dimensions is defined with

$$n = \frac{i_x B_z}{ed V_H} \tag{1.61}$$

Considering that the sample is low dimensional, the thickness *d* is neglected and the carrier concentration in two dimensions (sheet carrier density) is obtained as

$$n_{2D} = \frac{i_x B_z}{e V_H} \tag{1.62}$$

From Eq. (1.62) using the current and magnetic field values applied on the main bar of a Hall bar and measuring Hall voltage, carrier concentration can be found. Re-arranging Eq. 1.62 using Eqs. 1.54-1.55 we obtain

$$\frac{i_x B_z}{edV_H} = \frac{i_x}{wdeE_x\mu_e} \tag{1.63}$$

And then μ_e is expressed as

$$\mu_e = \frac{l V_H}{B_z w V_x} \tag{1.64}$$

V_x represents the potential difference along x-axis, and l represents the length of the main arm. From Eq. 1.64 by knowing the applied magnetic field and applied voltage and, measuring Hall voltage, it is possible to determine the Hall mobility of the carriers.

1.5.2. High Field Regime: Landau Levels

As see in Figure 1.12, the movement of the carriers in the two-dimensional system is limited in the growth direction of the semiconductor structure. The carriers are located at discrete energy levels called subbands and their movement in the plane perpendicular to the growth direction. Total energy of a carrier in a subband with energy E_i is defined as

$$E(k_x, k_y, i) = \frac{\hbar^2 k_x^2}{2m^*} + \frac{\hbar^2 k_y^2}{2m^*} + E_i \tag{1.65}$$

The first and second terms on the right side of the Eq. 1.65 represent the motion of the electron in 2DEG plane.

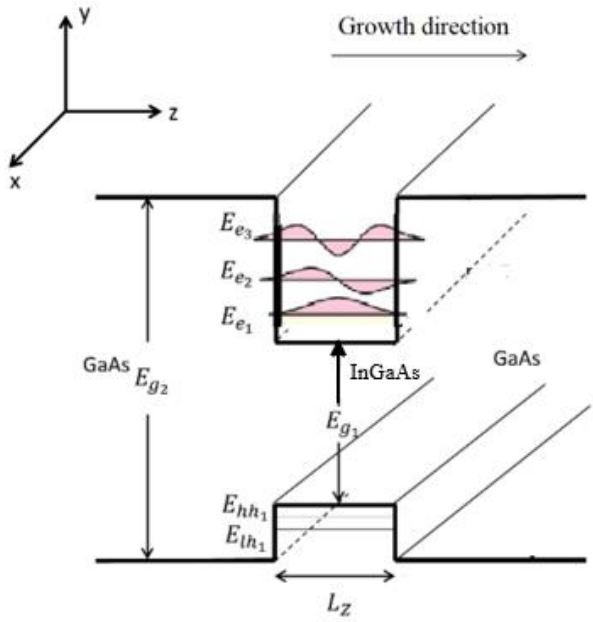

Figure 1.12: Schematic representation of a InGaAs/GaAs QW structure [31].

After applying magnetic field B_z (in z direction) perpendicularly to the 2DEG system, the first energy levels of the electrons are split into Landau levels. The energy of the electron in the presence of a magnetic field is described as

$$E(N, i) = \hbar\omega_c(N_L + \frac{1}{2}) + E_i \tag{1.66}$$

where N is the Landau quantum number, and $\hbar\omega_c$ is the difference between Landau levels. ω_c is the cyclotron frequency and defined as,

$$\omega_c = \frac{eB}{m^*} \tag{1.67}$$

If magnitude of magnetic field is enough to affect the spin energy level, each Landau level is split in two as a result of the spin of the electron ($\pm\frac{1}{2}$) . The energy of these levels is [49] ,

$$E_s = sg\mu_B B \tag{1.68}$$

μ_B represents the Bohr magneton, g represents the effective g-factor and depends on the magnitude of the magnetic field. When the spin related splitting is taken into account, the energy of electron under an applied magnetic field is written as [48]

$$E(N,i,s) = \hbar\omega_c\left(N_L + \frac{1}{2}\right) + E_i \pm \frac{1}{2}g\mu_B B_z \tag{1.69}$$

Eq. 1.69 reveals that, as the value of the applied magnetic field increases, the frequency of cyclotron increases, so the difference between Landau levels increases. As the magnetic field increases as seen in Figure 1.13a, the allowed states, which are uniformly distributed when the magnetic field is zero, turn into a series of δ-functions with the same distance $\hbar\omega_c$ from the continuous states.

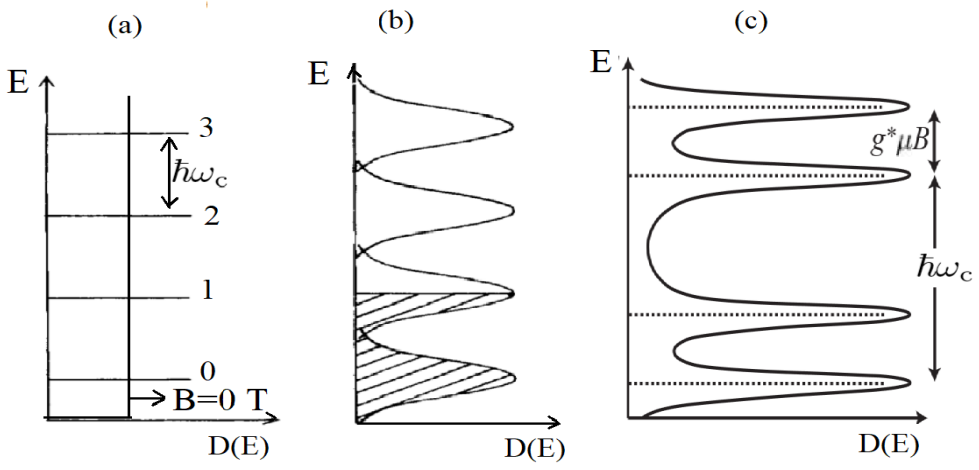

Figure 1.13: Density os states at a) B > 0T, b) B > 0T and at the presence of scatterings and c) B >> 0T and at the presence scatterings [48].

Landau levels are discrete in only an ideal case, but in real materials, there are fluctuations in spatial potential as a result of random order of impurity atoms. The electrons scatter from these fluctuations, and the time between two consecutive scatterings is quantum lifetime of electrons. Since the mean free path of electrons is finite, a degeneracy is formed at Landau levels and the Landau levels broadens as shown in Figure 1.13b [33]. Figure 1.13c shows density of states for electrons in a magnetic field under applied magnetic field.

The Landau levels are broadened by scatterings at spatial potential fluctuations of 2D electron gas. This effect can be seen as the influence of scatterings at potential fluctuations limiting the lifetime of an electron in a certain quantum state. As a result, the ideal delta- shaped density of states is broadened. The broadening of Landau levels is described in term of quantum lifetime as

$$\delta E = \frac{h}{\tau_q} \tag{1.70}$$

In the presence of the scatterings, Landau levels are shown in Figure 1.14 and the straight line is the sum of these Landau levels

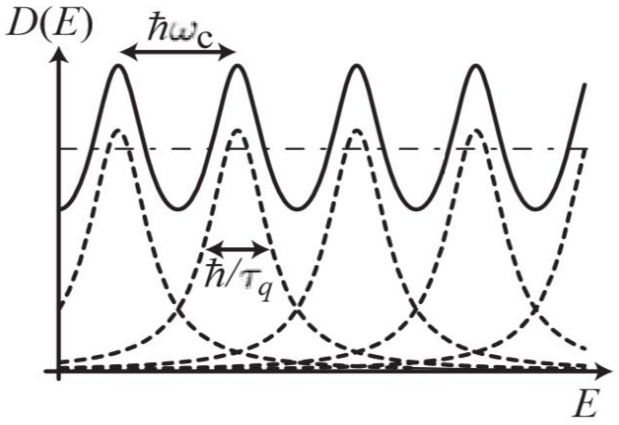

Figure 1.14: The density of state *versus* energy in presence of magnetic field and scatterings [48].

When the difference between the two Landau levels is less than $\frac{\hbar}{\tau_q}$where the condition $\omega_c \tau_q < 1$ is satisfied, Landau levels can be defined by Gaussian or Lorentzian type functions. Under this condition, the density of state function $\Delta g\ (\mathrm{E}, \mathrm{B})$ at 0K can be written as [66]

$$\frac{\Delta g(E,B)}{g_0} = \frac{g(E,B-g_0)}{g_0} = 2\sum_{r=1}^{\infty} exp\left(-\frac{\pi r}{\mu_q B}\right) cos\left[\frac{2\pi(E_F - E_i)}{\hbar\omega_c} - \pi r\right] g_0 \quad (1.71)$$

where g_0 defines the density of sates at 0T, r is harmonic number and μ_q is quantum mobility. The relation between quantum mobility and quantum lifetime is expressed as

$$\mu_q = \frac{e\tau_q}{m^*} \quad (1.72)$$

1.5.2.1. Landau level in graphene

The Landau levels in a 2DEG, obeying the Schrodinger Eq. with an effective mass, was given by Eq.

$$E(N,i) = \hbar\omega_c(N_L + \frac{1}{2}) \quad (1.73)$$

In the case of a single layer graphene, the Landau levels are given by [57]

$$E_N = \mp\sqrt{2e\hbar v_F^2 B N_L} = \mp\hbar\omega_G\sqrt{BN_L} \quad (1.74)$$

$N_L = 0,1,2,3, \ldots..$

where ω_G is the cyclotron frequency of graphene given by

$$\omega_G = \frac{\sqrt{2}\,\upsilon_F}{l_B} \quad (1.75)$$

And

$$l_B = \sqrt{\frac{\hbar}{eB}} \quad (1.76)$$

where the magnetic length l_B is the length scale of the cyclotron motion at a given magnetic field [22]. In both cases, N_L = 0, 1, 2, . . . It should be noted that in contrast to the standard 2DEG whose Landau levels are equally spaced, in a single-layer graphene, Landau levels depend on energy with the root of the index N_L.

It is interesting to note that the lowest Landau level occurs at energy of E = 0 eV. On the other hand, in Eq. (1.73) for a quasi 2DEG at $N_L = 0$ produces a non-zero energy level. This difference actually leads to an anomalous quantum Hall effect in graphene. The Landau level at zero energy is a unique characteristic of graphene band structure. As show in Figure 1.15, it leads to the maximum resistivity- at zero charge carrier density.

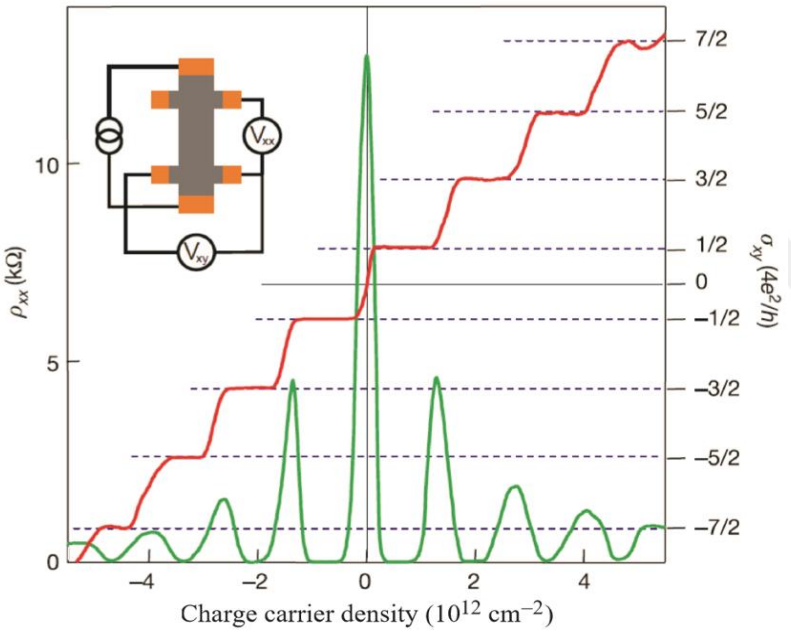

Figure 1.15: The longitudinal resistance (ρ_{xx}) and Hall conductivity (σ_{xy}) of a single layer graphene depending on the charge density when the magnetic field value is 14 T [22].

1.5.2.2. Shubnikov de Haas Oscillations

In low dimensional semiconductor systems, with the increase of the applied magnetic field on the semiconductor, the energy difference between two successive Landau levels increases. Landau levels expand and approach to Fermi level, and if the magnetic field intensity is sufficient, Landau levels pass through Fermi level. As a result, oscillations occur at the state density at the Fermi level. These oscillations are called Shubnikov-de Hass (SdH) oscillations.

A phase shift of is observed in SdH oscillations in graphene compared to conventional quasi 2D electron systems. This phenomenon is associated with massless Dirac fermions in graphene.

Longitudinal resistance R_{xx} measured in 2D electron system under a magnetic field can it is expressed as

$$R_{xx}(B) = \rho_M(B) + \rho_{osc}(B) \tag{1.77}$$

where $\rho_M(B)$ is the non-oscillating part of the magneto-resistance, and $\rho_{osc}(B)$ represent the SdH oscillations and is expressed for only single subband occupation as [73]

$$\frac{\Delta\,\rho_{xx}}{\rho_0}\alpha\sum_{i=1}^{\infty}D(r\chi)\exp\left(\frac{-i\pi}{\omega_c\tau_q}\right)cos\left[\frac{2\pi i(E_F-E_1)}{\hbar\omega_c}-i\pi\right] \tag{1.78}$$

where $\Delta\,\rho_{xx}$, ρ_0 , E_1, E_F , ω_c and τ_q are oscillatory part of magneto resistivity, magnetic-field resistivity, first subband energy, Fermi energy, cyclotron frequency and quantum lifetime, respectively. Whereas i represents the subbands. Here $\exp\left(\frac{-i\pi}{\omega_c\tau_q}\right)$ represent the damping because of Landau level collision broadening and

$$D(r\chi) = \frac{\chi}{sinh\chi} \tag{1.79}$$

with

$$\chi = \frac{2\,\pi^2 k_B T}{\hbar\omega_c} \tag{1.80}$$

describes the temperature damping. In Eq. 1.79

$$\mu_q = \frac{e\,\tau_q}{m^*} \tag{1.81}$$

and

$$\omega_c = \frac{e\,B}{m^*} \tag{1.82}$$

Using Eqs. from 1.78 to 1.82, and by the effective mass, temperature and magnetic field the thermal damping can be specified [73]

$$\frac{A(T,B_n)}{A(T_0,B_n)} = \frac{Tsinh(2\pi^2 K_B T_0 m^*/\hbar e B_n)}{T_0 sinh(2\pi^2 K_B T m^*/\hbar e B_n)} \tag{1.83}$$

The effective mass m^* can be found analysing the temperature dependence of the SdH amplitudes at a given magnetic field using Eq. 1.83. In Eq. 1.83 $A(T,B_n)$ and $A(T_0,B_n)$ are the amplitudes of the SdH oscillation peaks at a magnetic field of B_n and at temperatures T and T_0.

The analysis of SdH oscillations is also useful to determine both 2D carrier density and Fermi level. A plot of the reciprocal magnetic field $\left(\frac{1}{B_n}\right)$ against the peak number gives the period of the SdH oscillations, $\Delta_i\left(\frac{1}{B}\right)$. For each subband, the carrier density n_{2D} can be calculated from SdH oscillations using

$$\Delta_i\left(\frac{1}{B}\right) = \frac{e}{\pi\hbar n_{2D}} = \frac{e\hbar}{m^*(E_F - E_i)} \tag{1.84}$$

where $(E_F - E_i)$ represent energy difference between the Fermi level and first subband occupied level. The Fermi energies $(E_F - E_i)$ can be calculated using Eq.1.84 together with m^* that obtained from Eq.1.83.

2. MATERIALS AND METHODS

2.1. SAMPLE STRUCTURES

2.1.1. Quasi- 2D Sample Structure : n-type modulation doped InGaAs/GaAs QW structures

In this study, n-type modulation doped InGaAs/GaAs QW samples were grown at two different temperatures 475ºC and 580℃ to investigate the effect of growth temperatures on electronic transport properties. These examples were grown as reference examples to compare the electronic transport mechanism of the N-containing samples. For this reason, growth process was carried out at two different temperatures: the low temperature (475ºC) at which the crystal quality of the nitrogen-containing structures was obtained the best and the optimum temperature (580℃) of the GaAs-based samples. Within the scope of this study, it is also aimed to examine the growth temperatures and the electronic transport mechanisms of the samples after the heat treatment. The samples were subjected to $600s$ heat treatment at 700℃ to examine the effects of heat treatment and the duration of this heat treatment on the structure.

In the nomenclature of the samples as TNLB and TNH, the letter "T" represents Tampere University of Technology, where the samples were grown. The letter “N” is for doping type as an n-type. The letter "B" characterizes $600s$ heat treatment. "L” and "H" represent the (low growth temperature) and (high growth temperature), respectively. All of the samples were grown by MBE method at Tampere University Optoelectronics Research Centre [49] .

The sample structure is given in Figure 2.1. The samples were grown on a semi-insulating (SI) GaAs substrate, that does not affect its electrical properties and acts as a passive substrate. The structure consists of a n-type doped GaAs barrier and undoped InGaAs layer that form the QW. Dopant concentration (N_D) is $10^{18}cm^{-3}$. GaAs layers were grown at 580℃, while the InGaAs layer forming QW were grown at 475℃ for TNLB and 580℃ for TNH. Modulation doping was obtained by growing an undoped spacer GaAs layer with a thickness of 5nm between the doped barrier layer and QW in order to spatially separate the carriers passing through the QW from the barrier with their ionized parents in the barrier and weaken the Coulomb interaction between them.

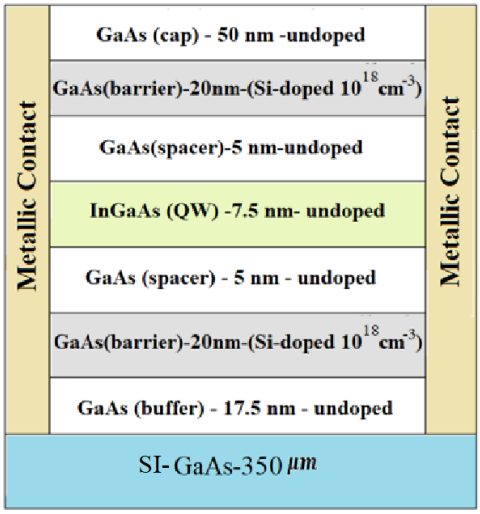

Figure 2.1: Structure of the quasi 2D sample.

Photolithography is one of the most common lithographic techniques used in fabrication of semiconductor materials. Photolithography technique was used to obtain Hall bar geometry. During fabrication or photolithography process we utilized well-known recipe in literature [72]

Using conventional photolithography techniques, we obtained Hall bar geometry as seen in Figure 2.3. Samples have been prepared in Hall bar form and simple bar geometries with lengths of $L = 1.75mm$ and width of $w = 0.2mm$.

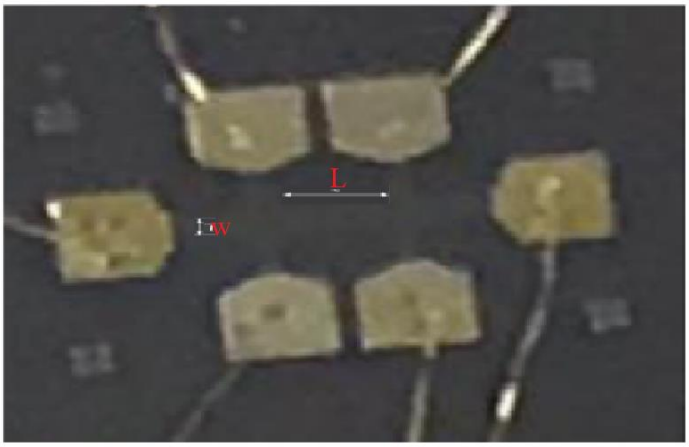

Figure 2.2: Optical microscope image of the Hall bar shaped sample.

2.1.2. Graphene Sample Structure

Single layer graphene sample structure SLG/TiO_2 /Si are given in Figure 2.3. The sample was grown at Bilkent University Graphene was first grown on copper sheets by CVD (Chemical Vapour Deposition) method. CVD is a widely used technique for growing larger size graphene. Graphene was first grown on a copper sheet using the CVD method. Then, the graphene on the copper sheet was taken from the furnace and cooled. A spin coating was made on graphene with a polymer polymethyl methacrylate (PPMA) to support graphene. The copper leaf was then removed using an abrasive ferric chloride (FeCl3). In this way, it ensured that only the graphene attached to the polymer remained. In the next step, graphene adhered to the polymer was transferred onto 300 nm thick substrate. By using acetone that can dissolve the polymer, graphene sample on TiO_2 / Si substrate was obtained. Using Raman measurement, graphene was confirmed to be single layer [60].

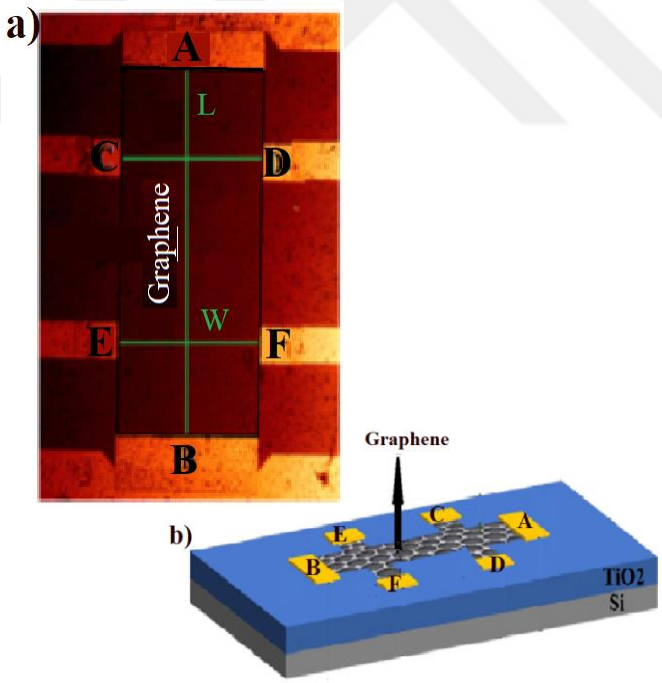

Figure 2.3: a) Optical microscope image of the fabricated Hall bar of single layer graphene b) An illustration of the Hall bar of a single layer graphene.

In the fabrication stage, a photomask for Hall bar geometry was designed and used in order to make transport measurements using Hall bar geometry. Ohmic contacts were made by reverse lithography technique. After this step, titanium and gold, respectively, having a thickness of 20

nm, 100 nm, were allowed to precipitate onto the sample by electron beam evaporator. The standard lift-off procedure was followed. Mesa lithography was performed to protect the active area of graphene by eroding the rest of the graphene on the substrate with O_2 plasma. After etching, a Hall bar with $w = 500\mu m$ and$L = 1000\ \mu m$ was obtained as shown in Figure 2.4

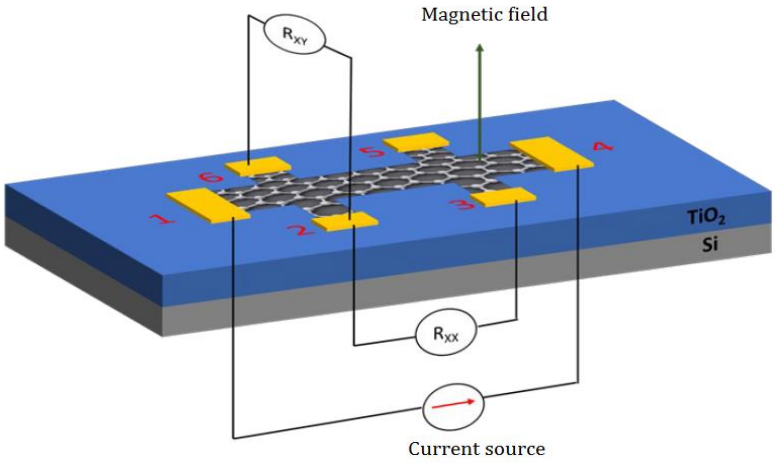

Figure 2.4: Graphene sample in Hall Bar geometry on TiO_2 / Si substrate.

2.3. EXPERIMENTAL METHODS

2.3.1. Hall Effect Measurement

Hall Effect measurement setup was used to perform Hall effect measurements. The sample was placed within a cryostat and measurement was taken from the six arms of the Hall bar as show in Figure 2.5. The measurements were made at temperatures between 77K to 300K. Electric field was created by applying constant current on main arm with Keithley 2400 Sourcemeter. The Hall voltage was measured between the arms perpendicular to main arm with Keithley 199 DMM. The temperature was controlled by the temperature control unit (Oxford ITC4). Before starting the experiment, I-V (current voltage) measurement were carried out to define optimum current value. Also, we carried out magneto-resistance measurement to inspect the effect of magnetic field on the Hall voltage and sample voltage. Then we made a decision comparing both I-V and V_H-B in which we observe linear behaviour to determine optimum constant current and magnetic field value. The current value should be chosen as small as so that the sample does not heat up, and magnetic field do too, but their value should high enough to measure stable voltage/current values.

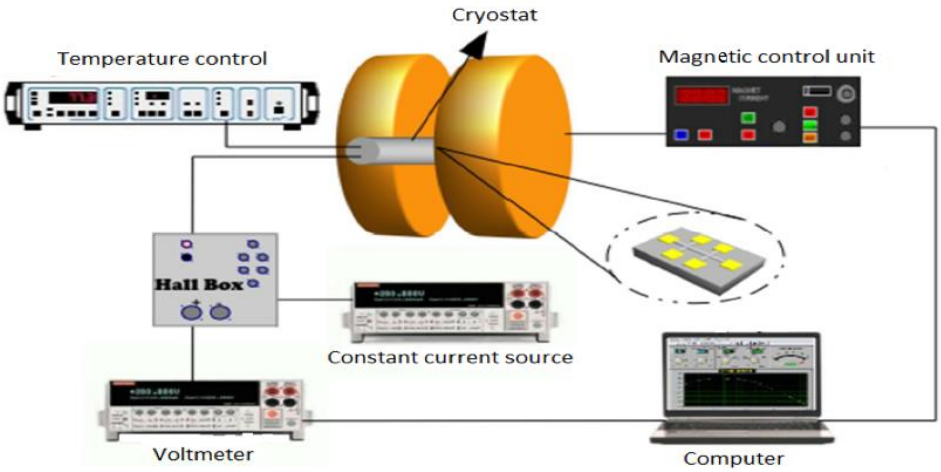

Figure 2.5: Hall effect set up [49] .

2.3.2. Magnetotransport Measurements

In the magnetotransport measurements, the sample prepared as Hall bar was placed in the cryostat between the superconductor coils (Oxford Superconducting Magnet 18T) so that the magnetic field lines are perpendicular to sample. The Oxford Heliox VL system has a ^{3}He cooling system and goes down to a temperature of 250mK. A constant current is passed over the main arm (A-B) and the sample voltage and Hall voltage were read at the same time with Keithley 2400 Source Meter. The temperature was controlled using Oxford ITC Mercury Temperature Controller. In Figure 2.6, the experimental setup used in the measurements is given.

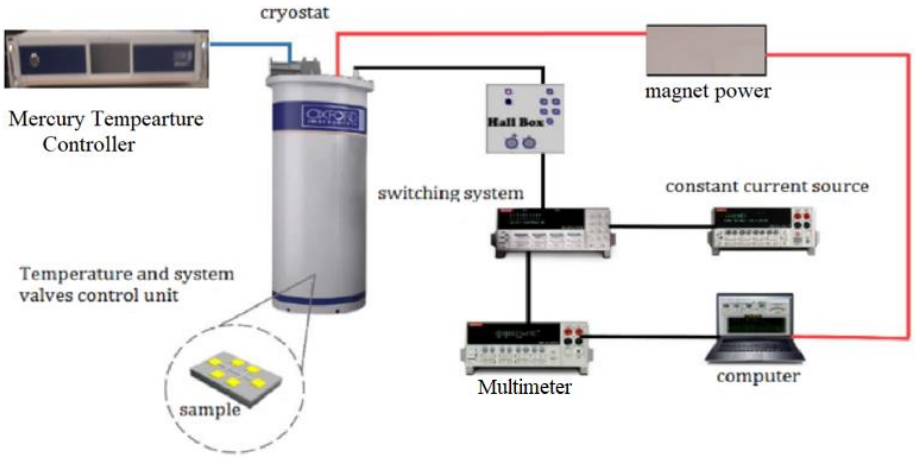

Figure 2.6: Experimental set-up of magnetotransport measurements [49] .

3. RESULTS

3.1. INGAAS/GAAS MODULATION DOPED STRUCTURES

3.1.1. Hall Effect Measurement Results

As mentioned in Section 2.7.1 firstly, V_H-I and V_H-B measurements were carried out to determine the constant current and magnetic field values to be applied during the measurements. From Figures 3.1 and 3.2, linear behaviour region and the considering best signal-to-noise, B=0.4 T and I= 0.05mA were chosen for the measurements for TNL sample. Both negative and positive magnetic field were applied and both directions of the current were used and an average values of Hall voltages were determined.

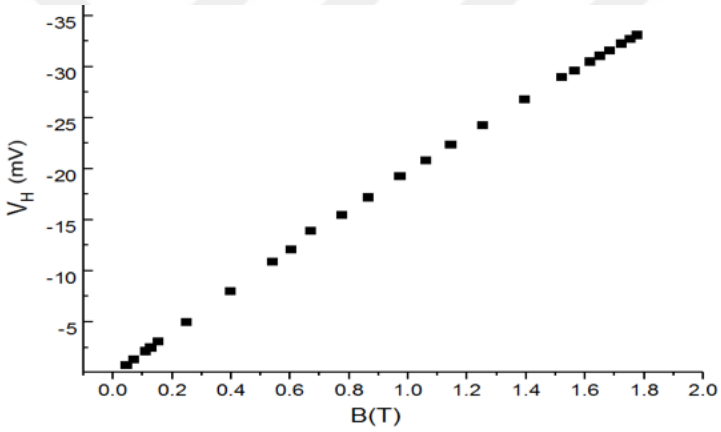

Figure 3.1: Hall voltage *versus* magnetic field at a fixed current

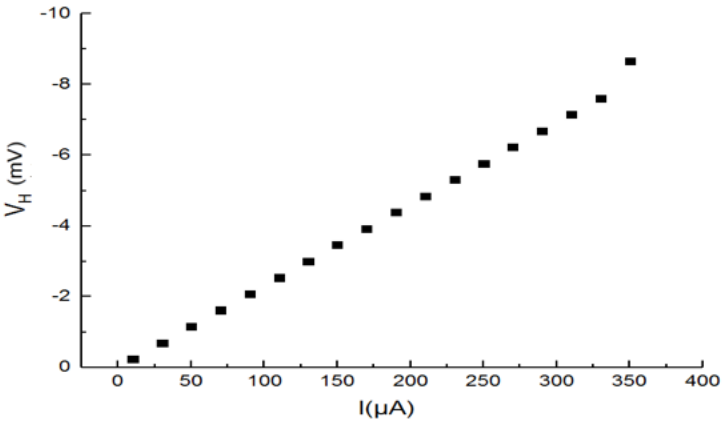

Figure 3.2: Hall voltage *versus* current at a fixed magnetic field

Hall measurements were made to determine carrier mobility and carrier concentration under a constant magnetic field in the temperature range of 4.2 to 300K.

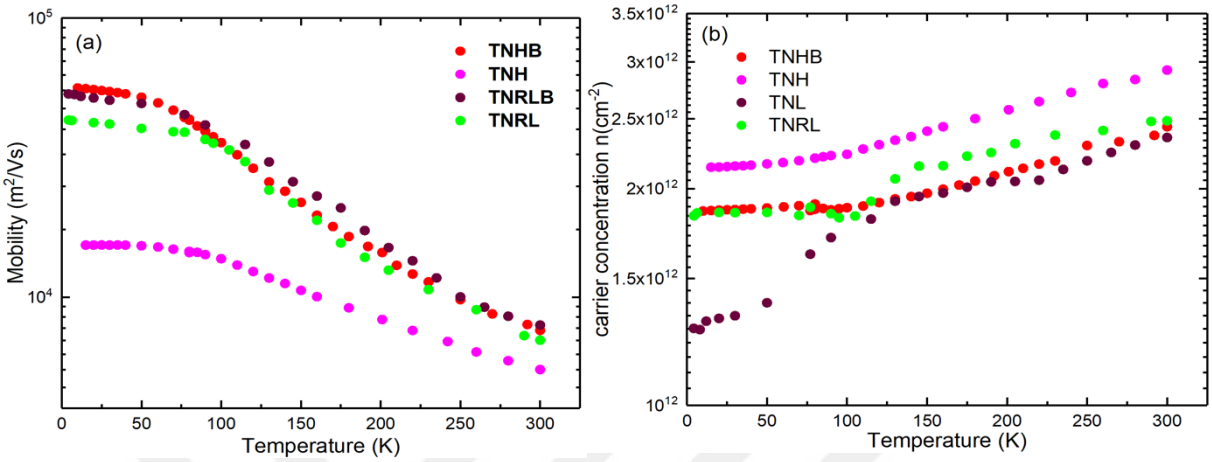

Figure 3.3: a) Hall mobility *versus* temperature b) Carrier concentration *versus* temperature.

Figure 3.3 a-b shows the temperature dependent mobility and electron density of as-grown and annealed samples, respectively. The temperature dependence of the electron mobility exhibits the well-known characteristic of modulation doped structures. At low temperatures (T<77K), electron mobility is almost temperature independent where ionized impurity scattering is dominant in conventional doped heterostructures. Thanks to the modulation doping, observed that the mobility is very high for all samples at temperature lower than 77 K. As temperature increases electron mobility decreases. The highest mobility (43121 cm^2/Vs) for as-grown samples are observed for low temperature growth sample (TNL) at low temperatures (T < 100K) and the lowest mobility (15362 cm^2/Vs) belongs to the high temperature growth as-grown samples (TNH) even it was grown at almost optimum growth temperature for InGaAs alloy. After annealing process, electron mobility of high temperature growth samples enhanced and almost become equal with the mobility of as-grown and annealed low temperature growth sample's electron mobility. It is obvious that thermal annealing does cause a slight improvement at all temperature range of interest for low temperature growth sample. After annealing low temperature electron mobility is almost the same for both low and high growth samples. Therefore, it can be said that annealing has a drastic effect for high temperature growth sample. The temperature-dependent carrier concentration changes of samples with and without heat treatment are shown in Figure 3.3b. Considering the TNH sample, a slight gradual increase in

carrier concentration with increased temperature is observed where the highest value is recorded $2.92 \times 10^{12} cm^{-2}$ at 300K. After thermal annealing, we note a decrease in carrier concentration to $2.4 \times 10^{12} cm^{-2}$ at 300K.

To comparing effect of growth temperature and also thermal annealing on carrier mobility, analytical calculations of temperature dependent mobility changes of as- grown and annealed samples are given in Figure 3.4 with considering all possible scattering mechanisms. For all samples coded, the low temperature electron mobility is restricted by mainly alloy and interface roughness scattering mechanisms. Whereas scattering caused by polar optical scattering dominates the mobility in the high temperatures. As mentioned in Section 1, the interface roughness scattering is typically resulted from two parameters, the lateral size (Δ=1.9*a for TNH and 1.3*a for TNLB) and the correlation length (Λ),which is used as adjustable parameters to fit the experimental data. In addition, the alloy potential was used to determine the alloy disorder scattering mechanism. The values obtained are given in Table 3.1. with the values for reference sample.

Table 3.1: Alloy potentials and correlation lengths for samples n-type $In_{0.32}$ $Ga_{0.68}$ As.

Sample code	U_{Alloy} (eV)	Λ (nm)
TNL	0.445	1.3
TNLB	0.300	0.9
TNH	0.537	29.8
TNHB	0.483	0.7

The best match between experimental and calculated value for electron mobility is obtained at low temperatures for all samples, as given in Figure 3.4. Whereas, the best match obtained over all temperature range was in as-grown samples. In annealed samples, a slight deviation between experimental and calculated mobility was observed at temperatures higher than 77K. Also, increasing in electron mobility is slightly was observed after heat treatment. From Figure 3.4, we note a decreases contribution for alloy disorder scattering and interface roughness scattering after thermal annealing. The optimum electronic transport properties with the lowest alloy potential and correlation length is observed for the low temperature growth sample and

following the thermal annealing reduced the interface roughness for this sample. Since the mobility is the lower for the sample grown at higher temperature, thermal annealing is more effective on the smoothing interface therefore a significant enhancement is observed for annealed high temperature sample. Table 3.2 shown variable parameters used for calculation.

Table 3.2: Variable parameters [44,49].

Parameter	Value
Optical phonon energy in GaInAs, $\hbar\omega_{po}$ (meV)	34
Optical phonon energy in GaAs, $\hbar\omega_{po}$ (meV)	35
Longitudinal acoustic phonon velocity, v_L(ms^{-1})	5087
Deformation potential, Ξ (eV)	7.32
Static dielectric constant, $\varepsilon_s(\varepsilon_0)$	13.9
High frequency dielectric constant, $\varepsilon_\infty(\varepsilon_0)$	11.11

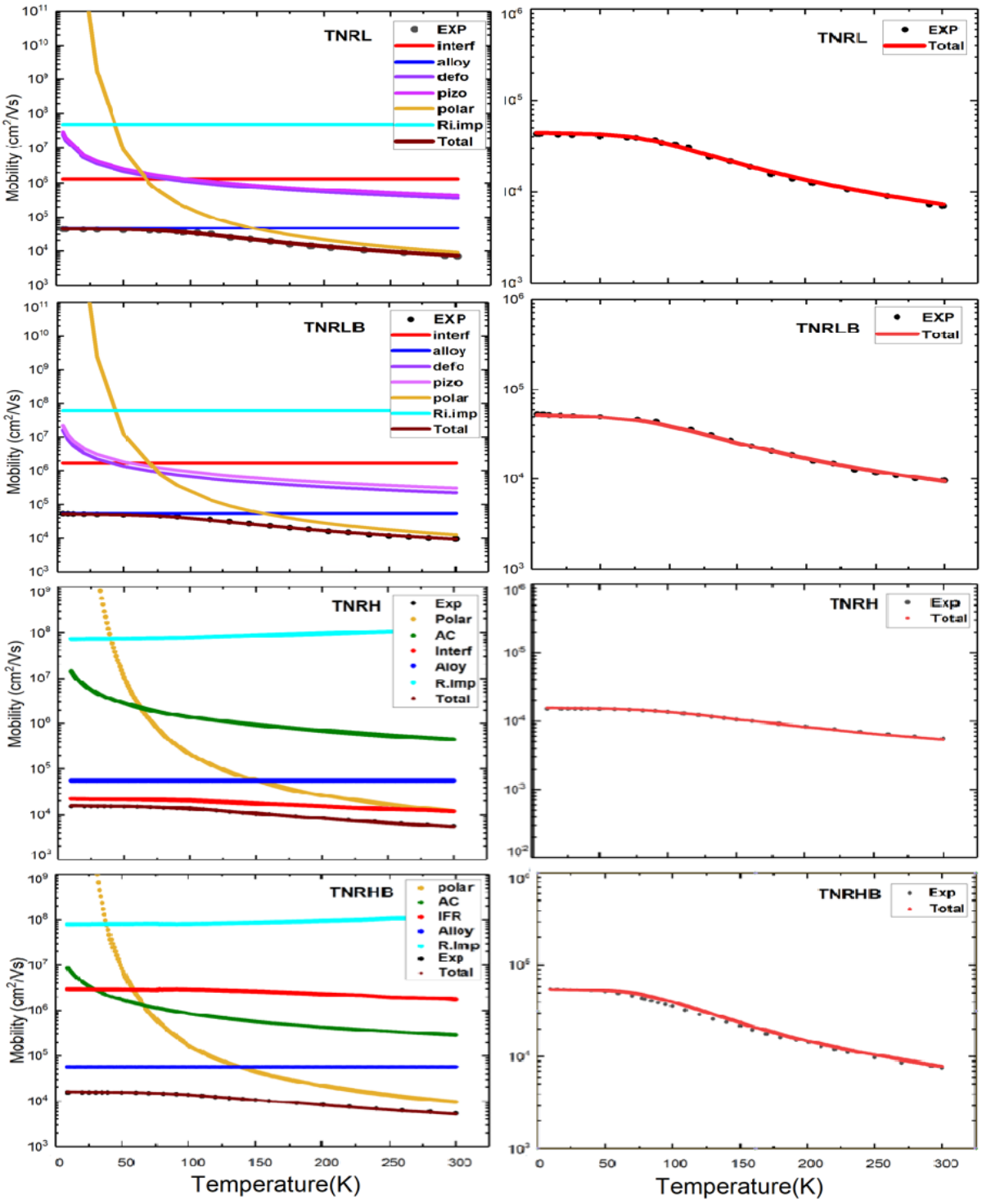

Figure 3.4: Analytical calculation of the temperature-dependent mobility of the samples.

It has been reported that for In compositions greater than 0.2, InGaAs growth on GaAs results in In surface segregation at high temperature growth. And thermal stability of InGaAs QW material requires low temperature growth at around 400-500^{o}C, on the other hand GaAs barrier

material has to be grown at higher temperatures (around 580°C) [66] and [67]. A strong temperature dependence of In segregation is revealed for InGaAs/GaAs QW structures with a segregation length more than 30Å at temperatures above 600°C [67]. And the surface segregation of In atoms drastically limits to achieve perfect abrupt interface between GaAs and InGaAs [67]. Several methods have been used to solve this problem, but the growth of high quality InGaAs/GaAs QW structures is still a challenge. Therefore, we have observed higher electron mobility for the sample grown at lower temperature, but applying thermal annealing is found to be a solution to enhance mobility for high temperature growth InGaAs/GaAs QW structures.

3.1.2. Magnetoresistance Results

Figure 3.5 shows the magnetoresistance experimental data $R_{xx}(B)$ measured at different temperatures for all samples. SdH oscillations clearly appear at very low magnetic fields because the electron mobility values are so high for all samples. The measurements on low temperature growth and high temperature growth samples were taken at two different systems with different maximum magnetic fields being 7T and 18T. Therefore, magnetic field values are different.

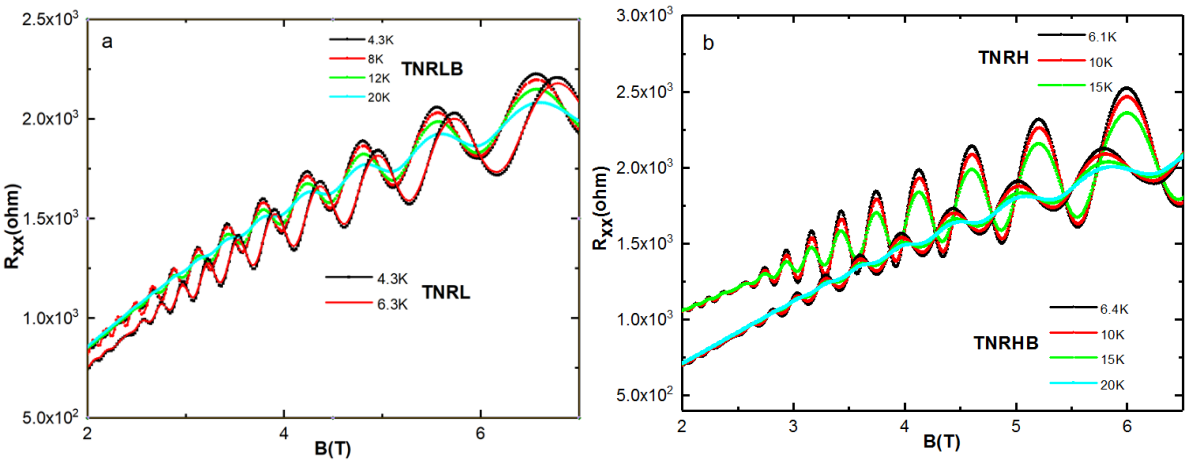

Figure 3.5: Raw experimental magnetoresistance of a) TNR, TNLB. b) TNH, TNHB.

The characteristic of magnetoresistance curves for low temperature growth as-grown (TNL) and annealed (TNLB) samples are complicated and both the period of oscillation and the shape of oscillations change with increasing magnetic field. Experimentally observed

magnetoresistance are the sum of classical magnetoresistance and SdH oscillations. To eliminate background magnetoresistance the negative of second derivative of the raw magnetoresistance data with respect to the magnetic field $\left(-\frac{\partial^2 R_{xx}}{\partial B^2}\right)$ are taken and shown in Figure 3.6. The SdH oscillations in the second derivative of magnetoresistance have well defined envelopes. As seen from Fig. 3.5, the magnetoresistance curve for high temperature growth samples have a linearly increasing classical magnetoresistance background with increasing magnetic field for the as-grown sample. For the annealed high temperature growth sample (TNHB), a slight deviation from linearity is observed above approximately 4T. On the other hand, the background magnetoresistance characteristic has a linearity below 3.5T and quite deviates from linearity above 3.5T. Therefore, to be able apply this second derivation method, only low magnetic field range (<4T) is used for the samples apart from TNLB. As for TNLB, even at the low magnetic field range it was impossible to fit the oscillations using standard expression given by 1.79, but it is obtained well-defined SdH oscillations at higher magnetic field range as seen in Figure 3.6b. However, the magnetoresistance curves become more complicated at higher magnetic fields as can be seen in Figure 3.5a with an anomalous background magnetoresistance. Even the data is used to determine transport parameters of TNLB, we do not believe that these parameters cannot be compared with the transport parameters of other samples because they cannot be obtained at the similar magnetic field range.

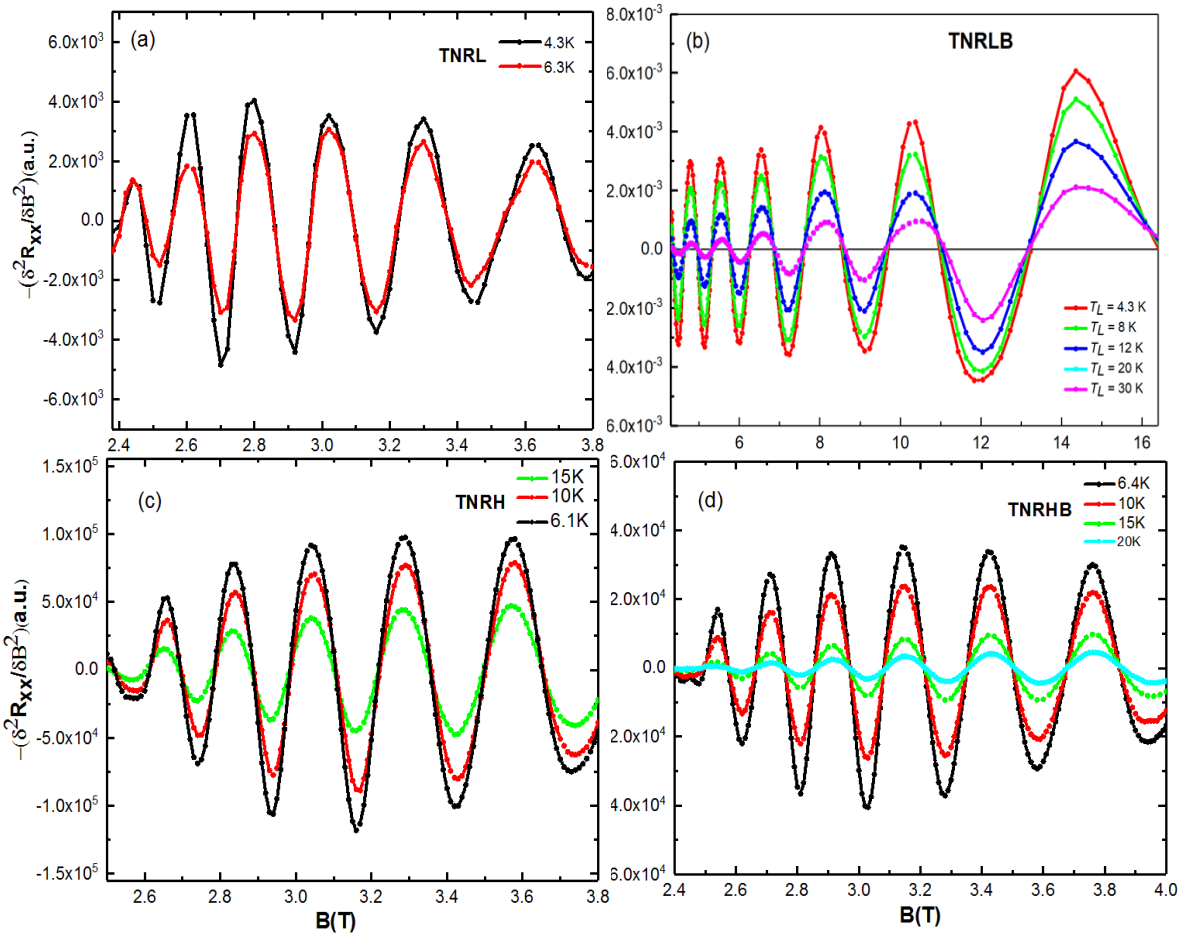

Figure 3.6: Second derivative of the SdH oscillations at different temperatures for. a) TNRL b) TNLB. c) TNH. d) TNHB.

SdH is used to obtain both 2D carrier density and Fermi level. The period of the SdH oscillations has been obtained from a plot of the reciprocal magnetic field $\left(\frac{1}{B}\right)$ against the peak number. which yields the oscillation period $\Delta_i\left(\frac{1}{B}\right)$. By using equation 1.84 the 2D carrier density we can determine in addition to Fermi energy for each sample. Figure 3.7 shows a plot of $\left(\frac{1}{B}\right)$ *versus* peaks number for two samples.

Effective electron mass values were obtained by proportioning the amplitudes of the SdH oscillations given in Figure 3.6 at a given magnetic field value and using Eq. 1.83. The values

obtained from the analysis of SdH oscillations are given in Table 3.3. Enhancement in effective mass have been observed after thermal annealing.

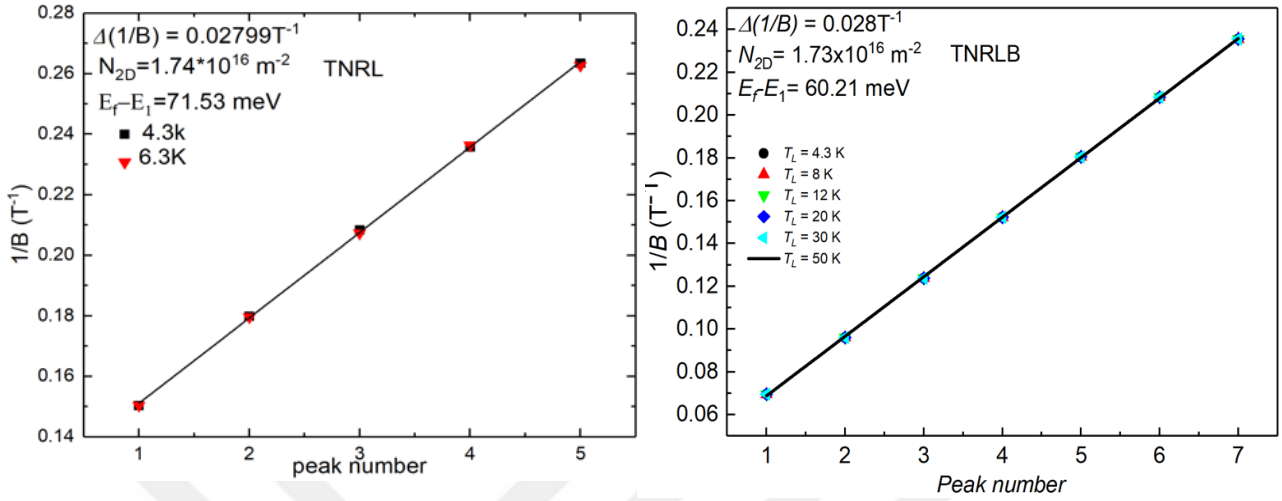

Figure 3.7: Plot of 1/B *versus* peak numbers for TNL and TNLB.

Table 3.3: Carrier density, Fermi level and effective mass values obtained using SdH oscillations.

Sample	$n_{SdH}(\times 10^{12}\ cm^{-2})$	$(E_{f-}E_i)(meV)$	m* (m_0)
As-grown TNL	1.74	71	0.057
Annealed TNLB	1.73	60	0.070
As-grown TNH	2.02	122	0.050
Annealed TNHB	1.92	82	0.055

As seen from the calculated transport parameters given in Table 3.3, as-grown low temperature growth sample (TNL) has the lowest 2D carriers and the highest effective mass. Since the effective mass is larger, density of states is higher, therefore Fermi level is smaller than those

for as-grown and annealed high temperature growth samples. We exclude TNLB from the discussion because the analysis of this sample was able to at higher magnetic fields than the others. The 2D carrier density is the highest for TNH and the effective mass is the smallest, which results in the highest Fermi level. When the sample is annealed, 2D carrier density decreases and effective mass increases. The effective mass values become comparable for as-grown low temperature growth and annealed high temperature growth samples.

3.2. GRAPHENE SAMPLE (SLG/TIO_2/SI)

The I-V curve of the single layer graphene is given at Figure 3.8. Using the inverse slop of the I-V curve (Figure 3.8), the resistance of the sample at room temperature is determined to be 19Ω .

3.2.1. Hall Effect Results

As mentioned earlier for the quasi 2D samples, sample was mounted and placed within a cryostat and measurement was taken from some arms of the Hall shaped bar. Before starting the experiment, the current (I) and constant magnetic field (B) were measured to determine the constant current and constant magnetic field values to be used in the experiments. From Figures 3.9, linear behaviour and the considering best signal-to-noise, B=0.8 T and I= 0.01mA were chosen for the measurements. Both negative and positive magnetic field were applied and both directions of the current were used an average values of Hall voltages were determined.

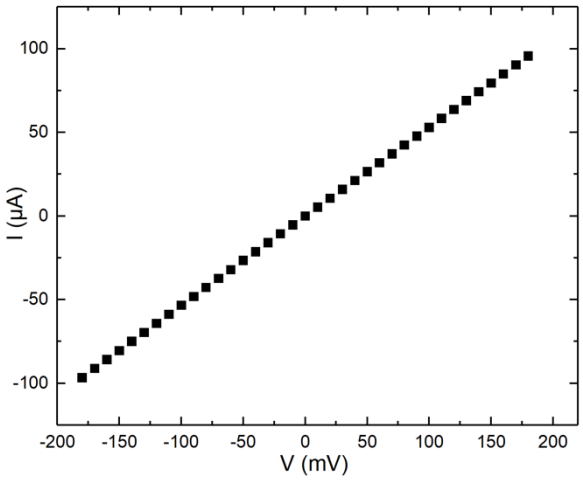

Figure 3.8: I-V measurement at room temperature

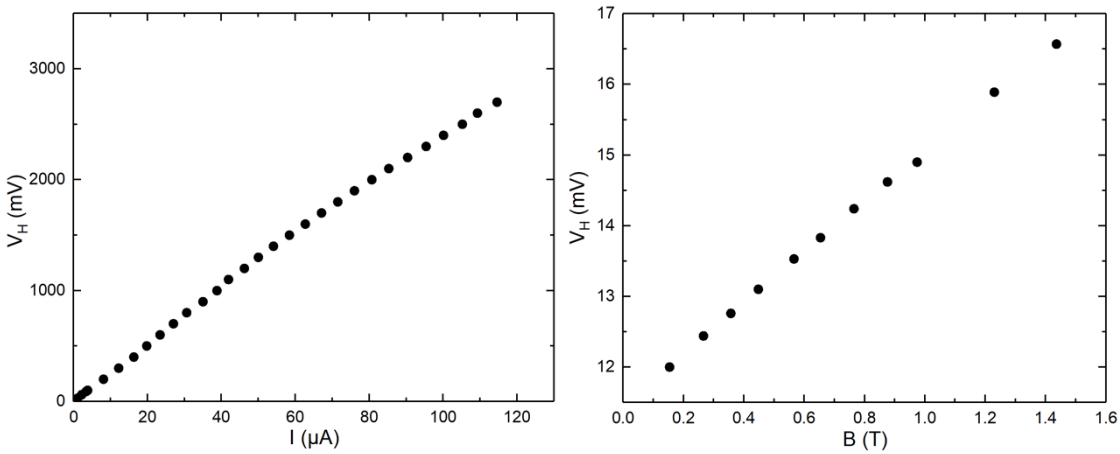

Figure 3.9: a) Hall voltage *versus* applied current at a fixed magnetic field and b) Hall voltage *versus* magnetic field at constant current.

For the SLG / TiO_2 / Si sample, the temperature dependent mobility has been investigated in temperature range of 77-300K in addition to Hall carrier density. The temperature dependent carrier mobility is shown in Figure 3.10 under a magnetic field of 0.8 Tesla. The mobility decreases with increasing temperature then, at around 125K, jumps to a higher mobility value. With increasing temperature, mobility decreases. The observed unexpected low temperature dependent mobility characteristic (a sharp decrease then a jump to higher mobility) is the reason to repeat the experiment fourth times until we observe a stable temperature characteristic of mobility. At the third and fourth measurements, it is observed almost the same characteristic.

As seen from the repeated experiments, mobility is increased after the first experiment and the characteristic of mobility curve changed. At low temperatures, mobility decreases with increasing temperature, then at around 175K an increase is observed. At temperatures between 170K-240K, it is observed almost temperature independent characteristic of mobility. Above 240K, mobility decreases as an effect of phonon scatterings. The jump to higher electron mobility values at around 125K at the first measurements almost disappears with the repetition times of the experiment, but another small jump appears at around 175K for all three measurements. This can be related with removal of scattering centres originating from various impurities on graphene surface as the sample is heated by applied current during the measurements.

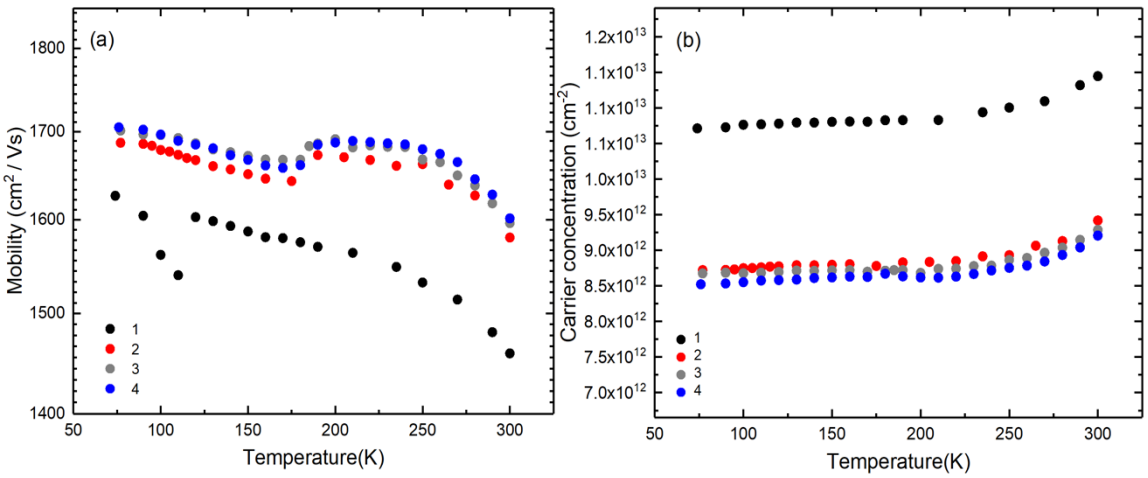

Figure 3.10: a) Temperature dependence of a) Hall mobility and b) carrier concentration

Temperature dependence of the 2D carrier density is found to be almost temperature independent as can be seen in Figure 3.10b. The 2D electron density is the highest at the first measurement. Whereas, the mobility was lowest value from other measurements. When the experiments are repeated, 2D carrier density decreases and the mobility becomes higher for the lowest 2D carrier density. Above 175K, the observed slight increase in 2D carrier density and the phonon scatterings results in decrease in the mobility. A slight increase in 2D carrier density above 175K can be related to thermally excited impurities in either TiO_2 substrate or graphene. It has been shown that properties of graphene can be drastically affected from the ambient conditions due to adsorption of water, oxygen, hydrogen and ammonia affects. Because of graphene films have point and line defects, the adsorption of small molecules can be resulted with destructive chemical attack. It has been reported that graphene line defects can be split fragments at temperatures as low as 90K as an effect of water. Besides, adsorbed water can split graphene [68]. It has been reported that molecules/atoms such as water, nitrogen and helium etc. can penetrate the interface between substrate and the single graphene layers and reduce the free carrier density from substrate . Therefore, graphene is very sensitive to ambient conditions, where humidity, oxygen can react with graphene. The adsorption of water can be utilised to tailor the bandgap of graphene [68] or results in p- or n-type doping [15]. It has been reported that adsorption of humidity molecules or oxygen may result in increasing free electron density of graphene. K. Elibol *et al.* investigated the effect of water on graphene and they observed that water adsorption increases 2D electron density and decreases mobility due to impurity

scattering [69]. Under the light of reported effects of ambient conditions on graphene in the literature, we may say that the observed higher 2D density and the lowest mobility characteristic at whole temperature range of interest at the first experiment can be related to donated electron to graphene from adsorbed humidity molecules or oxygen. When the experiments are repeated without removing the sample from the cryostat it may be said that applying electric field may cause to desorption of ambient molecules from the surface of the graphene, resulting in an increase of 2D electron mobility of graphene and decrease of electron density for all temperature range.

The last experiment measurements (fourth) was selected to analytical modelling, because it has the lowest s-shape characteristic of temperature dependence of the mobility. The scattering mechanisms affecting the mobility of the carriers in the graphene sample have been evaluated with every possible scattering mechanism mentioned in Section 1.4.2. as shown in Figure 3.11. The theoretical scattering mechanisms that limit the mobility of the carrier are fitted to the experimental mobility data using Matthiessen's rule. From the Figure 3.11 and apart from bulk ionized impurity scattering. The bulk remote impurity scattering has given unrealistically high mobility for the measured 2D carrier density, therefore it was not included to analyses, so the factors affecting mobility at low temperature region is temperature independent scattering event limit the mobility. Remote interface phonon scattering (μ_{RIP}) and longitudinal acoustic phonon scattering (μ_{LA}) are the dominant at high temperature, in addition to temperature independent mobility (μ_0). The temperature-independent mobility limiting term is found as $1687\ cm^2/Vs$. In the calculation of the remote interface optical phonon (μ_{RIP}) mobility given by Eq. 1.48, the energies of the optical phonons on the surface and bottom surface of graphene were taken as $E_1 = 70meV$, $E_2 = 20meV$. The parameters used in the calculations are given in Table 3.3.

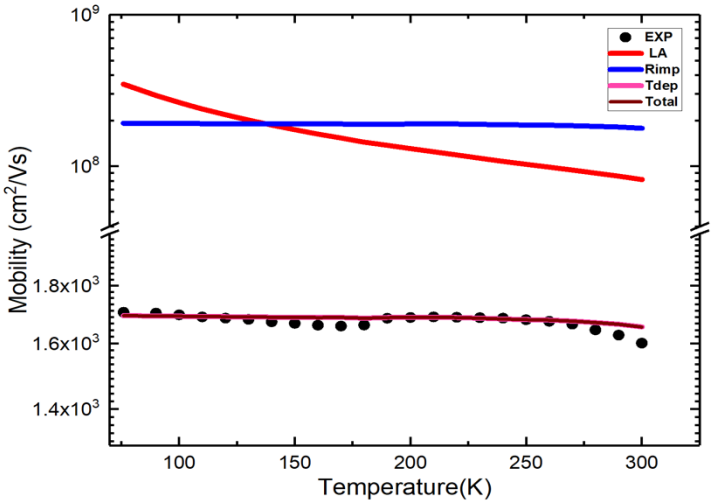

Figure 3.11: Analytical calculation of the temperature-dependent mobility of SLG/TiO_2/Si sample, considering with all possible scattering mechanisms

The observed mobility value for SLG/TiO_2/Si has slightly lower than the reported values for epitaxial growth SLG/SiC [62] and CVD growth SLG/ SiO_2/Si [70] even TiO_2 has the higher dielectric constant than SiC and SiO_2. The higher dielectric constant screen the effect of impurity potential but make dominant RIP scatterings. On the other hand, the reported 2D carrier densities of these two sample is lower than that in SGL/TiO_2/Si, which causes the electron mobility lower

Table 3.4: Parameters used in analytical calculation of possible scattering mechanisms restricted temperature dependence of mobility [62,43].

Parameter	Value
Deformation Potential, (D_A (eV)	30
Mass Density, ρ_s $(\times 10^{-7}\ kg/m^2)$	7.7
Fermi Velocity, v_s $(\times 10^4\ \ m/s)$	2.1
Longitudinal Acoustic Phonon Velocity, v_F $(\times 10^6\ \ m/s)$	1.0
Effective Mass, m^* $(m_0\ )$	0.053
Static Dielectric Constant, $(\varepsilon_s\ )$	70
permeability of empty space, ε_0 (F/M)	8.85×10^{-7}

3.2.2. Magnetoresistance Results

The magnetotransport measurements were taken at another system with 18T superconductive magnet. Therefore, the sample was taken out of the Hall effect system to the ambient conditions. When the sample was place in 18T superconductive magnet system, the resistance of the sample was measured quite high in MOhm range. In the 18T superconductive magnet, a ^{3}He sample-in-vacuum dipstick insert system with the sample holder is used and the sample holder is kept under high vacuum in an inner vacuum can (IVC) tube before pulling down the insert into the LHe dewar. Then, to make enable the thermal contact between the dewar and the Heliox insert, ^{3}He gas is given to the IVC therefore the sample is exposure to the ^{3}He gas. It has been reported that He atoms can penetrate towards to the interface between substrate and the graphene layer and caused a decrease in 2D carrier density, avoiding the contribution from substrate to the graphene layer. More helium atoms more reduced 2D carrier density [71]. The reason to observed drastic increase in the resistance of the sample can be attributed to this effect. The magnetoresistance result at 4.2K are given Figure 3.12. The data is very noisy and it impossible to take the data from Hall bar arms. It was not observed any SdH oscillations, which is a confirmation of non 2D characteristic. When the measurement is repeated by applying higher current, the resistance increased more not be measurement with current measurement set-up. Therefore, magnetoresistance measurement to determine electronic transport parameters of the single layer graphene could not be carried out. When the sample was taken out from the system, it was seen that there was no problem with the wiring of the sample, but the single layer graphene probably damaged.

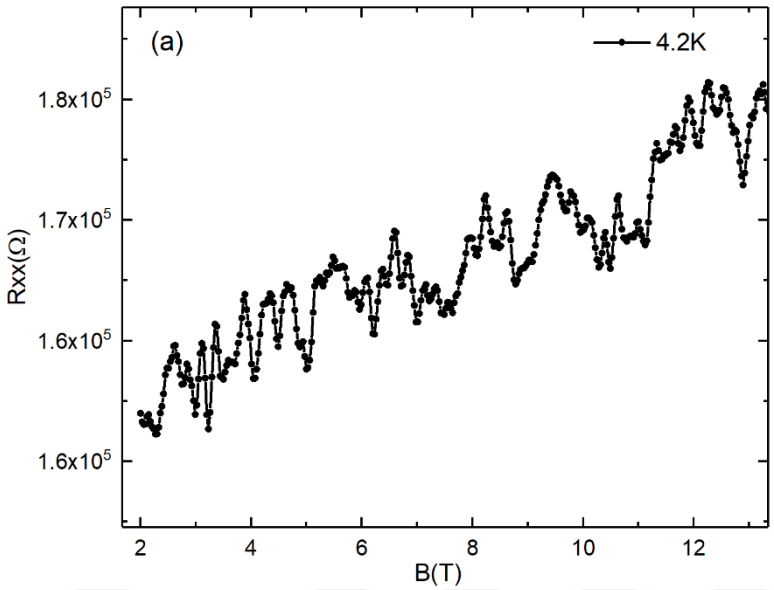

Figure 3.12: a) Magnetoresistance measuerement of SLG/TiO_2/Si at 4.2K.

4. DISCUSSION

The result obtained has been already discussed in Results section together with experimental results. Therefore, discussion of the results is briefly presented here. In the first part of the thesis, electronic transport properties of the quasi 2D samples, QW structures grown at low and high temperatures has been investigated. Hall effect and magnetransport measurement were carried out on as-grown and thermal annealed low and high temperature growth samples. The temperature dependence of the electron mobility has been analyze using an analytical method. In the analysis, all possible scattering mechanisms have been considered. The low temperature electron mobility is observed to almost temperature- independent, which is a characteristic of 2D electron gas. With increasing temperature, electron mobility in all samples decreases. The highest low temperature mobility has been observed for low temperature growth quasi 2D sample and electron mobility is observed to be slightly increases following thermal annealing. As for high temperature growth as-grown sample, the low temperature electron mobility is found to the lowest among all samples' electron mobility. After thermal annealing, the electron mobility enhanced and reached the low temperature electron mobility of the low temperature growth samples. I have been mentioned in Results section, growth process of InGaAs QW materials on GaAs barrier material causes In segregation at the interface at high temperature growth [66,68]. Therefore, we observe that electron mobility at low temperature is higher for low temperature growth sample. Even high temperature growth samples suffer from In segregation, our results indicated that thermal annealing can be used to improve the electron mobility in high temperature growth sample. From Figure 3.3-a we note that the mobility at low temperatures almost constant below 75 K a result of reduced the effect of remote ionized-impurity scattering as mentioned in section 1.2. As we see from Figure 3.4, remote ionized-impurity scattering-limited electron mobility is almost flat. So, at low temperature region the mobility almost temperature-independent. Also, this result refers to that the electron mobility of 2D electron gas is determined by temperature insensitive scattering mechanisms such as alloy disorder scattering and interface roughness scattering. But at around 100 K the contribution from polar optical phonon scattering increases with increasing temperature and the electron mobility decreases. The temperature dependence of electron mobility obeys the characteristic of the quasi 2D modulation doped heterostructures. The effect of the other scattering mechanisms as acoustic phonon scattering with both (deformation potential and piezoelectric

effect) and remote ionized-impurity scattering on the electron mobility are much smaller comparing with interface scattering and alloy scattering.

For the as-grown samples, the electron mobility for the low temperature growth sample (TNL) is higher than that in TNH because of smaller correlation length, which lead to reduce in the interface roughness scattering, so increase in the electron's mobility. After the heat treatment, the observed increase in the low temperature electron mobility is explained with reduced interface roughness via decreased correlation length. Also, it has been found that the quality of material increased by heat treatment whereas, decrease alloy potential. Therefore, even the electron mobility is low in high temperature growth sample, the mobility can be tuned by annealing.

The magnetotransport measurements have revealed an oscillatory characteristic with an increasing magnetoresistance background. The SdH oscillations have started at very low magnetic fields. The background magnetoresistance has observed not to have a linear characteristic. As the magnetic field is increased, the background magnetoresistance deviates from its classical linear characteristic. To remove the background magnetoresistance from the magnetoresistance curves, second derivative is taken in the case of having a classical linear magnetoresistance characteristic. Here, we used this technique to be able to analyses SdH oscillations to obtain effective mass, Fermi level and 2D carrier density values. Only the range of having linear magnetoresistance change is meaningful to use classical analysis of SdH oscillations. Therefore, we had to analyses SdH oscillations at different magnetic field regions. Analysis of the as-grown and annealed high temperature growth an as-grown low temperature growth sample could be made at the similar magnetic field range, but for annealed low temperature growth sample we had to use higher magnetic field region, which resulted in incomparable values of especially effective mass and we excluded this sample's results from the others to make a comparison among the samples. The effective mass values of the as-grown low temperature growth and annealed high temperature growth samples are found to be almost the same. Since the 2D electron densities are higher for high temperature growth samples, Fermi levels are found to have higher for high temperature growths samples. Since the effective mass value is smaller and the 2D electron density is higher, Fermi level is higher for the high temperature growth as-grown sample *via* lower density of states. The low temperature growth

sample has the lowest 2D electron density and the highest effective mass value, resulting in higher density of states therefor Fermi level is found to be the lowest for this sample.

For graphene, being a real 2D structures, classical Hall effect measurements were made in the temperature range of 77K to 300K under magnetic field 0.8 Tesla for the examination of electronic properties for graphene (SLG / TiO_2 / Si) sample. The results have revealed that ambient conditions drastically effect the electron mobility in graphene. As we have repeated the experiments we have observed an increase in electron mobility for all temperature range and 2D electron density decreased, as we repeated the experiments until consistent results were obtained. The change in electron density and electron mobility have been explained with possibility of the presence of humidity molecules on the graphene. Besides, an anomalous temperature dependence of 2D electron mobility like an S-shape has been observed, which can be related to activation of defect levels at the temperature range of 175K.

The theoretical mobility curve was fitted to experimental mobility data by using theoretical mobility calculations. The most probable scattering mechanisms reported in the literature were used to fit the experimental data. We observed that scattering from longitudinal acoustic and remote interface phonons at the high temperatures were the dominant scattering mechanisms. For the remote interface phonon scattering (μ_{RIP}), optical phonon energy in graphene is much higher than the thermal energy at room temperature. So, it is expected that the effect of the optical phonon on electronic transport is very limited. [44]. Considering the thickness of the single layer graphene, which is to small comparing to substrate, if substrate optical phonon energy is close to thermal energy at high temperature, the layer on graphene should be affected by substrate optical phonon, which causes scattering of charge carriers in graphene, leading to remote interface phonons (μ_{RIP}).

As mentioned in section 3.3, for the longitudinal acoustic phonon scattering (μ_{LA}), as a result of absent of the polar optical phonon scattering in graphene, which lead to high mobility in room temperature and this mobility limited only by acoustic phonon scattering through weak deformation-potential coupling. So longitudinal acoustic phonon scattering (μ_{LA}), is dominant at high temperatures. As a result of uncertainty in the precise quantitative value of deformation-potential coupling constant D_A, the range of D_A is taken from the literature [44].

Last scattering mechanism have been observed is temperature independent mobility, which includes short range scattering and Coulomb scattering where the 2D electron mobility is 1688 cm^2/Vs in whole studied temperature range. And this scattering maybe related to the interaction between graphene and substrate [45]. In the magnetotransport measurements, as mentioned in section 3.2.2, after finishing Hall effect measurement, the sample was taken to the magnetotransport system for measurements, it's probable that sample adsorbed some oxygen from environment and also adsorbed Helium gas, which was given to the insert of the system to establish a thermal equilibrium with outside LHe temperature of the dewar's LHe space. Therefore, the sample resistance changed from Ohm range to the almost GOhm range than when we repeated the experiment applying higher current, the resistance became much higher. At the first run of the experiment, we could manage to measure noisy magnetoresistance without any SdH oscillations, which is an indication of not having 2D electron gas system, but then since the resistance was so high (it was not reversible when we took out the sample from the system.), neither magnetoresistance nor Hall effect at 4.2K could not be measured

5. CONCLUSION AND RECOMMENDATIONS

Electronic transport properties of modulation doped n-type ($In_{0.32}Ga_{0.68}As/GaAs$) quantum well (QW) structures (quasi-2D structures) and single-layer graphene on TiO_2/Si substrate (real-2D) structures have been investigated. The quasi 2D samples has been annealed for 600 s at 700°C.

First, we have study electronic properties for InGaAs/GaAs QWsamples that were grown at low and high temperatures in terms of carrier mobility, carrier density, effective mass, and scattering mechanism that limits electron mobility. We observed the highest electron mobility for TNL sample that grown at low temperature. The interface roughness for TNRL sample compare to the others, was found to be the less. For all samples the alloy disorder scattering and interface roughness scattering are the prevailing scattering mechanisms. It is found that the alloy potential takes value of 0.445 eV for TNRL. While, it was 0.537 eV for TNH. After thermal annealing, improvement in carrier mobility was observed. Following thermal annealing process, a decrease in the correlation length was obtained, therefore it was concluded thermal annealing decreases interface roughness.

From the Shubnikov-de Haas (SdH) oscillations, 2D carrier density, the effective mass and Fermi energy in n-type ($In_{0.32}$ $Ga_{0.68}As/GaAs$) QW structures have been calculated. The effective mass has been extracted from the temperature dependence of the SDH amplitude at constant magnetic field. From periods of the SdH oscillations, carrier density and Fermi energy were obtained.

For graphene, Hall carrier mobility and carrier concentration depending on temperature were determined from classical Hall measurements that were made in the temperature range of 77 to 300K. An increase in electron mobility and decrease in 2D electron density were obtained at whole temperature of interest with repeated experiments Besides, we observed a change in electron mobility at 175 K where it can indicate that some carriers are trapped at some defect levels then thermally excited with increasing temperature. Different scattering mechanisms have been considered for evaluating the temperature dependence of the electron mobility in single layer graphene sample system. It was observed that scattering from longitudinal acoustic and remote interface phonons at the high temperatures were the dominant scattering

mechanisms as well as temperature independent mobility including short range scattering and Coulomb scattering has an effect on electron mobility at whole temperature range of interest.

When these two material systems are compared, graphene, which is a true 2D material, is superior to quasi 2D QW systems in terms of ease of production and simplicity of production methods. In quasi 2D QW systems, to obtain 2D electron gas, semiconductor layers with wide and narrow band gaps must be grown on a substrate successively. The growth processes of these structures, which are grown with epitaxial growth systems, are more difficult and time consuming, and the growth costs are very high. In terms of their fabrication, the production is similar for both 2D and real 2D materials, using photolithography or electron beam lithography. However, in the production of graphene with very small dimensions, aligning the single layer between the contacts makes the production process somewhat difficult. Although the same techniques are used to determine electronic transport properties, the measurements on the quasi 2D structures can be carried out more easily. Since graphene is a single layer material, the applied potential difference easily damages it. The graphene grown on SiC, which was planned to be used for the investigation of substrate effects within the scope of the thesis, was unfortunately damaged for this reason. During the studies, it has been observed that quasi 2D materials are quite stable and the measurements made on these materials are repeatable. However, graphene's properties differ depending on the ambient conditions, so it is not a very stable material yet. The scattering mechanisms that affect the electron mobility differ in real and quasi 2D materials. Being layered and alloyed, in addition to phonon, neutral impurity and remote ionized impurity scatterings, interfacial roughness and alloy potential fluctuation scattering mechanisms are also considered in InGaAs/GaAs QW systems. The scattering mechanisms that affect the mobility of electrons in graphene are less, but because it is grown onto a substrate and has a single atomic layer thickness, the substrate has a significant effect on electron mobility. In addition, impurities remain from the fabrication process deteriorates electron mobility.

REFERENCES

[1]. Zhores, A., Herbert, K., Jack, S., 2000, *Developing semiconductor heterostructures used* in *high-speed and opto- electronics*, https://www.nobelprize.org/prizes/physics/2000/, [Date of visit:15/02/2021].

[2]. Harris,E., Klitzing, K.,1987, *Physics and applications of quantum wells and superlattices*, Erice, Sicily, Italy ISBN: 0-306-42823-7

[3]. Esaki, L., Tsu, R., 1969, Superlattice and negative conductivity in semiconductors, IBM, *Research Note* RC-2418.

[4]. Stormer, H. L., Dingle, R., Gossard, W., Wiegmann,W., Sturge, D., 1979, Two dimensional electron gas at a semiconductor-semiconductor interface, *Solid state communication*, 29 (10), 705-709.

[5]. Charlier, J., 1990, *Characteristics of two-dimension electron gas in III-V compound heterostructures grown by MBE*, ISBN: 0-12-752130-5

[6]. Cankurtaran, M., Çelik, H., Tiras, E., Bayrakli, A., and Balkan, N., 1998 , Quantum and transport mobilities of electrons in GaAs/$Ga_{1-x}Al_xAs$ multiple quantum wells, *Solid state physics*, 207 (1), 139-146.

[7]. Klitzing, K. V., 2017, Quantum hall effect: Discovery and application, *The annual review of condensed matter physics*,8,13-30.

[8]. Cristian, R. D., 2014, *MBE growth of ultrahigh-mobility 2DEGs in GaAs/AlGaAs*, Thesis (PhD), Regensburg University, Germany.

[9]. Tiras, M., Cankurtaran, H., Çelik, A., Boland, T., Balkan, N., 2001, Magnetotransport in modulation-doped $In_{0.53}Ga_{0.47}As$/ $In_{0.52}Al_{0.48}As$ heterojunctions: in-plane effective mass and quantum and transport mobilities of 2D electrons, *Superlattices and microstructure*, 29 (2), 147-167.

[10]. Abdul, M. K., Mohammad, A. A., Christophe, G., 2021, 2DEG transport properties over temperature for AlGaN/GaN HEMT and AlGaN/InGaN/GaN pHEMT, *Microelectronic engineering, Elsevier*, 238, 111508.

[11]. Sonmez, F., Arslan, E., Ardali, S., Tiras, E., Ozbay, E., 2021, Determination of scattering mechanisms in AlInGaN/GaN heterostructures grown on sapphire substrate, *Journal of alloys and compounds*, 864,158895.

[12]. Sun, Y., Balkan, N., Erol, A., Arikan, M. C., 2009, Electronic transport in n- and p-type modulation-doped GaInNAs/Gas quantum wells, *Microelectronics journal, Elsevier,*40 (3), 403- 405

[13]. Gunapala, S., D., Bandara, S. V., Levine, B. F., Sarusi, G., Park, J. S., Lin, T. L., Pike,W., Liu, T. K.,1994, High performance InGaAs/GaAs quantum well infrared photodetectors, *Applied Physics letter,* 64 (25), 3431-3433.

[14]. Jasprit, S., *Semiconductor devices*, New York, Mc Graw Hill Book Co., ABD, ISBN: 0-07-113906-0.

[15]. Novoselov, K. S., Geim, K. Morozov, S. V., Jiang, D., Zhang, Y., Dubonos, S. V., Grigorieva, I.V., Firsov, A., 2004, Electric field effect in atomically thin carbon films, *Science,* 306 (5696), 666-669.

[16]. Geim, A. K., Novoselov, K. S., 2007, The rise of graphene, *Nature Material*, 6 (3), 131-191.

[17]. Charlier, J.C., Eklund, P. C., Zhu, J., Ferrari, A. C., 2008, Electron and phonon properties of graphene: their relationship with carbon nanotubes, Verlag Berlin Heidelberg, *Applied Physics Letters*, 111, 673-709.

[18]. Xuesong, Li., Weiwei C., Jinho A., Seyoung K., Junghyo N., Dongxing, Y., Richard, P., Aruna,V., Inhwa, J., Emanuel, T., Sanjay, K., Banerjee, L. C., Rodney,S. R.,2009, Large Area Synthesis of High-Quality and Uniform Graphene Films on Copper Foils, *Science,* 324, 1312-1314.

[19]. Lei, L., Yung, C. L Mingqiang, B., Rui, C., Jingwei, Ba., Yuan, L., Yongquan, Q., Kang, L.,Yu, H.,Xiangfeng, D.,2010, High-speed graphene transistors with a self-aligned Nano -wire gate, *Nature,* 467, 305-308.

[20]. Sukang, B., Hyeongkeun, K., Youngbin, L., Xiangfan, X., Jae-Sung, P., Yi, Z., jayakumar , B., Tian, L., Hye, R. K., Young, S., Young-Jin, K., Kwang, Jong-Hyun, A., Byung, H., Sumio, I., 2010, Roll-to-roll production of 30-inch graphene films for transparent electrodes, *Nature Nanotechnology*, 5, 574-578.

[21]. Bonaccorso, F., Sun, Z., Hasan, T., Ferrari, C.,2010, Graphene photonics and optoelectronics, *Nature Photonics*, 4, 611-622.

[22]. Dash, G. N., Satya, R., Sriyanka, B., 2014, Graphene for Electron Devices: The panorama of a Decade, *Electron devices Society*, 2 (5), 77-104.

[23]. Yan, Z., 2011, *Electronic transport properties of semiconductor nanostructures*, Thesis (PhD), Stony Brook University.

[24]. Sarma, S. D., Shaffique, A., Hwang, E. H., Enrico, R., 2011, Electronic transport in two-dimensional graphene, *Reviews of Modern Physics*, 83 (2), 407-471.

[25]. Yan, W. T., Horst, L. S., Philip, K.,2005, Experimental observation of the quantum Hall effect and Berry's phase in graphene, *Nature*, 438, 201-204.

[26]. Novoselov, K. S., Jiang, Z., Zhang, Y., Morozov, S. V., Stormer, H. L., Zeitler, U., Maan, J. C., Boebinger, G. S., Kim, P., Geim, A. K., 2007, Room-temperature quantum Hall effect in graphene, *Science*, 315 (5817), 1379.

[27]. Cenk, Y., 2016, *Fabrication and charge transport measurements on graphene-based nanostructures in the quantum hall regime*, Thesis (PhD), Sabancı University.

[28]. Zanato, D., Gokden, S., Balkan N, Ridley, B. K., Schaff, W. J.,2004, The effect of interf-face roughness and dislocation scattering on low temperature mobility of 2D electron gas in GaN/AlGaN, *Semiconductor science and technology*, 19 (3), 427-432.

[29]. Sakaki, H., Noda, T., Hirakawa, K., Tanaka, M., 1987, Matsusue, T., Interface roughness scattering in GaAs/AlAs quantum wells, *Applied Physics* letter, 51 (23), 1934-1936.

[30]. Zefram, D., 2014, *III-V Bismides as a new heterojunction material system for electronic Devices*, Thesis (PhD), University of Colorado Boulder.

[31]. Pallab, B., 2013, *Semiconductor optoelectronic device*, Delhi, ISBN: 978-013 4956565.

[32]. Jaro, M., Electronic properties of semiconductor alloy systems,1985, *Reports on progress in physics*, 48 (1985), 1091-1154.

[33]. Jasprit, S.,2003, *Electronic and optoelectronic properties of semiconductors*, Cambridge University Press, New York, ISBN: 978-0-511-07863-7.

[34]. Jörg, N., Chris, G. V., 1995, Electronic structure and phase stability of $GaAs_{1-x}N_x$ alloys, *Physical Review*, 51 (16), 10568-10571.

[35]. Vurgaftman, I., Meyer, J. R., 2001, Band parameters for III–V compound semiconductors and their alloys, *Applied physics review*, 89 (11), 5815-5875.

[36]. Herbert, K., 2000, Quasi-electric fields and band offsets: Teaching electrons new tricks, *International journal of modern physics*, 16 (5), 677-697.

[37]. Mark, F., 2007, *Quantum well, superlattices, and band-gap engineering,* Springer hand book of electronic and photonic materials, ISBN: 978-0-387-26059-4.

[38]. Harris, J., Pals, A., Woltjer, R., 1989, Electronic transport in low-dimensional structures, *Reports on progress in physics, Review*, 52, 1217-1266.

[39]. Schubert, E. F.,2006, *Foundation of solid-start devices*, Rensselear polytechnic institute, troy New York, ISBN: 0986382620.

[40]. Almamun, A., 2011, Quantum confinement an ultimate physics of nanostructures, *Encyclopedia of Semiconductor Nanotechnology*, 5, 1-67.

[41]. Yoffe, A. D.,1993, Low-dimensional systems: quantum size effects and electronic properties of semiconductor microcrystallites (zero-dimensional systems) and some quasi-two dimensional systems, *Advances in physics*, 42 (2), 173-262.

[42]. Mark, F., 2010, O*ptical properies of solids states*, Oxford university press, New Yourk, ISBN: 978–0–19–957336–3.

[43]. David, A., miller, B., 2003, Optical physics of quantum wells, Rm. 4B-401, AT&*T Bell Laboratories*, Holmdel, NJ07733-3030, USA.

[44]. Donmez, O., Sarcan, F., Lisesivdin, S. B., Vaughan, M. P., Erol, A., Gunes, M., Arikan, M. C., Puustinen, J., Guina, M.,2014, Analytic modeling of temperature dependence of 2D carrier mobility in as- grown and annealed GaInNAs/GaAs quantum well structures, *Semiconductor science technology*, 29,125009-13.

[45]. Kazuhiko, H., Hiroyuki, S.,1986, Mobility of the two-dimensional electron gas at selectively doped n-type $Al_xGa_{1-x}As$/GaAs heterojunctions with controlled electron concentrations, *Physical Review*, 33 (12), 8291-8303.

[46]. Kearney, M., Horrell, I.,1998, The effect of alloy scattering on the mobility of holes in a $Si_{1-x}Ge_x$ quantum well, *Semiconductor science technology*,13**,** 174-180.

[47]. Littlejon, M.A., Hauser, J., Glisson, T. H., Ferry,D., Harrison,1978, Alloys scattering and high field transport in ternary and quaternary III-V semiconductors, *Solid-stat electronic*, 21, 107-114.

[48]. Thomas, I., 2010, *Semiconductor nanostructures quantum states and electronic transport* ,Oxford University, New York, ISBN: 978–0–19–953442–5.

[49]. Fahretten, S., 2012, *Investigation of optical and electrical properties of modulation and*

doped GaInNAs/Gas quantum well structures, Master thesis, Istanbul University.

[50]. Magdalena, W., 2009, *Graphene: a two-type charge carrier system*, Master thesis, University of the Faculty of Mathematics and Natural Sciences.

[51]. Zang, H., 2011, *Electronic transport properties of semiconductor structure*, Thesis (PhD), Stoony Brook University.

[52]. Yong, Z., 2016, *Graphene heat spreaders for electronics thermal management application*, Thesis (PhD), Chalmers University of Technology.

[53]. Charlier, J.C., Eklund, P. C., Zhu, J., Ferrari, A. C.,2008, Electron and phonon properties of graphene: Their relationship with carbon nanotubes, *Applied physics*, 111, 673-709.

[54]. Peres, N. M., 2009, The transport properties of graphene, *Journal physics*: *Condensed matter*, 21, 323201.

[55]. Castro, A., peres, N. R., Novoselov, K. S., 2009, The electronic properties of graphene, *Reviews of modern physics*, 81(1), 109-162.

[56]. Sarma, D. S., Shaffique, A., Hwang, E. H., Enrico, R., 2011, Electronic transport in two dimensional graphene, *Reviews of modern physics*, 83 (2), 407-470.

[57]. Yue, Z., 2012, *Quantum hall transport in graphene and its bilayer*, Thesis (PhD), Columbia, University.

[58]. Michael, B., 2012, *Transport properties of nanostructures and superlattices on single-layer and bilayer graphene*, Thesis (PhD), Antwerpen University.

[59]. Tian, F., Aniruddha, K., Huili, X., Debdeep J., 2007, Carrier statistics and quantum capacitance of graphene sheets and ribbons, *Applied physics letters*, 91(9), 092109.

[60]. Hakan A., 2017, *Galvanomagnetic measurements in graphene samples*, Master Thesis, Anadolu University.

[61]. Kubakaddi, S. S., 2009, Interaction of massless Dirac electrons with acoustic phonons in graphene at low temperatures, *Physical review*,79 (7), 075417.

[62]. Lisesivdin, B., Atmaca, G., Arslan, E., Çakmakyapan, S., Kazar, Ö., Bütün, S., Ul-Hassan J., Janzén, E., Özbay, E.,2014, Extraction and scattering analyses of 2D and bulk carriers in epitaxial graphene-on-SiC structure, *Science direct*, *Elsevier*, 63, 87-92

[63]. Yu, C., Li, J., Liu, Q. B., Dun, S. B., He Z., Zhang, X. W., Cai, S. J., Feng Z. H., 2013, Buffer layer induced band gap and surface low energy optical phonon scattering in epitaxial graphene on SiC (0001), *Applied physics letter*,102 (1), 013107.

[64]. Wenjuan, Z., Vasili P., Marcus, F., Phaedon, A., 2009, Carrier scattering, mobilities, and electrostatic potential in monolayer, bilayer, and trilayer graphene, *Physical review*,80 (23), 235402.

[65]. Edward, M., P., David, J. M., 2013, *Electricity and magnetism,* Harvard University, Massachusetts, ISBN: 978-1-107-01402-02-2.

[66]. Toyoshima, T., Niwa, T., Yamazaki, J., Okamoto, A., 1993, In surface segregation and growth mode transition during In GaAs growth by molecular beam epitaxy, *Applied physics letters*,63 (6), 821-823.

[67]. Disseix, P., Leymarie, J., Vasson, Vasson, A. A. M., Monier, C., 1997, Optical study of of segregation effects on the electronic properties of molecular- beam- epitaxy grown (In,Ga) As/GaAs quantum wells, *Physical review*, 55 (4), 2406-2412.

[68]. Xiaofeng, F., Sabine, M., Miquel, S., 2012, Water Splits Epitaxial Graphene and intercalates, Journal of *American chemical society*, 134, 5662-5668.

[69]. Elibol, K., 2012, *Magneto conduction and facial properties investigations of graphene obtained by graphite stripping and epitaxial methods*, Master Thesis, Gazi University.

[70]. Tiras,E., Ardali, S.,Tiras, T., Arslan, E., Cakmakyapan, S., et al.,2013, Effective mass of electron in monolayer graphene: Electron-phonon interaction, *Journal applied physics*, 113 (4), 043708.

[71]. Nair, R. R., Wu, H., A., Jayaram, P. N., Grigorieva, V., Geim A., K., 2012, Unimpeded permeation of water through helium-leak-tight graphene-based membranes, *Science*, 335, 442-444.

[72]. Erman,Ç., 2017, *Electronic transport in III-N-V and III-Bi-V semiconductor alloy*, Master Thesis, Istanbul University.

[73]. Engin, T., Sukru, A., 2013, Electron and hole energy relaxation rates in GaInNAs/Gas quantum wells via deformation potential and piezoelectric scattering, *Solid state physics*, 250 (1), 134-146.

CURRICULUM VITAE

Personal Information	
Name Surname	Adal AB. MA. Rajhi
Place of Birth	
Date of Birth	
Nationality	
Phone Number	
Email	
Web Page	

Educational Information	
B. Sc.	
University	Al Fateh University
Faculty	Faculty of Science
Department	Physics Department
Graduation Year	1996

M. Sc.	
University	Belgrade
Institute	Institute of Electrical Engineering
Department	Physics
Programme	Electro-optical systems

Ph. D.	
University	İstanbul University
Institute	Institute of Graduate Studies in Science and Engineering
Department	Department of Physics
Programme	Physics Programme

Publications
Rajhi, A., Aydin, M., Çokduygulular, E., Çetinkaya, Ç., Donmez, O., Yildirim, S., Sarcan, F., Erol, A.,2018, Electronic transport in n-type modulation doped GaInAs/ GaAs and GaInNAs/GaAs quantum well structures, *Turkish Physical Society 34th International Physics Congress*, September 5-9, 2018, Bodrum/Turkey.